A twenty-year dataset of soil moisture and vegetation optical depth from AMSR-E/2 measurements using the multi-channel collaborative algorithm

Lu Hu, Tianjie Zhao, Weimin Ju, Zhiqing Peng, Jiancheng Shi, Nemesio J Rodríguez-Fernández, Wigneron J.-P., Michael H Cosh, Kun Yang, Hui Lu, et al.

Remote Sensing of Environment 292 (2023) 113595

Contents lists available at ScienceDirect

Remote Sensing of Environment

journal homepage: www.elsevier.com/locate/rse

A twenty-year dataset of soil moisture and vegetation optical depth from AMSR-E/2 measurements using the multi-channel collaborative algorithm

Lu Hu [a,b], Tianjie Zhao [c,*], Weimin Ju [a,d,**], Zhiqing Peng [c], Jiancheng Shi [e], Nemesio J. Rodríguez-Fernández [f], Jean-Pierre Wigneron [g], Michael H. Cosh [h], Kun Yang [i], Hui Lu [i], Panpan Yao [c]

[a] International Institute for Earth System Science, Nanjing University, Nanjing 210023, China
[b] School of Geography and Ocean Science, Nanjing University, Nanjing 210023, China
[c] State Key Laboratory of Remote Sensing Science, Aerospace Information Research Institute, Chinese Academy of Sciences, Beijing 100101, China
[d] Jiangsu Center for Collaborative Innovation in Geographic Information Resource Development and Application, Nanjing, Jiangsu 210023, China
[e] National Space Science Center, Chinese Academy of Sciences, Beijing 100190, China
[f] CESBIO, Université de Toulouse, CNES/CNRS/INRA/IRD/UPS, Toulouse, France
[g] INRAE, UMR1391 ISPA, F-33140 Villenave d'Ornon, France
[h] USDA ARS, Hydrology and Remote Sensing Laboratory, Beltsville, MD, USA
[i] Department of Earth System Science, Tsinghua University, China

ARTICLE INFO

Edited by Jing M. Chen

Keywords:
Soil moisture
Vegetation optical depth
MCCA
AMSR-E
AMSR2
Frequency and polarization dependence

ABSTRACT

Soil moisture (SM) and vegetation optical depth (VOD) are essential variables in the terrestrial ecosystem. The multi-frequency radiometers AMSR-E and AMSR2 provide >20 years of data records, enabling the development of long-term SM and VOD products. Most of the current retrieval algorithms either only focus on SM or VOD, and generally ignore the polarization or simplify the frequency dependence of vegetation effects for reducing the unknowns and facilitating the retrieval process, limiting the synergic applicability of VOD and SM products in the soil-plant-atmosphere continuum. In this study, a new global SM and frequency- and polarization-dependent VOD product from 2002 to 2021 was developed using the multi-channel collaborative algorithm (MCCA), based on the inter-calibrated AMSR-E/2 multi-frequency passive microwave measurements. The MCCA algorithm comprehensively considers the physical relationship between multiple microwave channels and could retrieve frequency- and polarization-dependent VOD while considering the accuracy of the SM retrievals. In the overall comparison with other SM products (AMSR-ANN, CCI-passive v07.1, LPRM-C/X, JAXA) over 25 dense SM networks, MCCA achieved the best scores in terms of root mean square error (RMSE = 0.074 m^3/m^3), unbiased root mean square error (ubRMSE = 0.073 m^3/m^3) and bias (0.007 m^3/m^3), and presented slightly lower value of Pearson's correlation coefficient (R = 0.709) than LPRM-X (R = 0.735). For the indirect evaluation of VOD with aboveground biomass (AGB) and MODIS NDVI, the MCCA product showed the performance comparable to other products (LPRM-C/X, VODCA-C/X/Ku). MCCA-derived VODs, especially for the H-polarized VODs, exhibited smooth non-linear density distribution with AGB and high temporal correlations with MODIS NDVI over most regions of the globe. In particular, MCCA-derived VODs can physically present reasonable variations across the microwave spectrum (values of VOD increase with microwave frequency), which is superior to the LPRM and VODCA products. It is expected that the MCCA algorithm can be extended to the observations of the ongoing AMSR2 or other similar satellite missions with multi-frequency capability, such as FY-3B/C/D/F/G or the upcoming AMSR3 and CMIR missions.

* Correspondence to: T. Zhao, State Key Laboratory of Remote Sensing Science, Aerospace Information Research Institute, Chinese Academy of Sciences, Beijing 100101, China.
** Correspondence to: W. Ju, International Institute for Earth System Science, Nanjing University, Nanjing 210023, China.
E-mail addresses: zhaotj@aircas.ac.cn (T. Zhao), juweimin@nju.edu.cn (W. Ju).

https://doi.org/10.1016/j.rse.2023.113595
Received 28 November 2022; Received in revised form 9 April 2023; Accepted 16 April 2023
Available online 23 April 2023

1. Introduction

Surface soil moisture (SM) plays a vital role in regulating water and energy exchanges between land surfaces and the atmosphere and is thus critically important for hydrological modeling (Houser et al., 1998; Wanders et al., 2014), agricultural management (Mohanty et al., 2017), and numerical weather forecasting (Drusch, 2007). Over the past few decades, passive microwave remote sensing has shown great advantages in monitoring SM at global or regional scales due to its high sensitivity to surface dielectric properties and frequent and continuous (all weather) monitoring of the Earth's surface. On the other hand, vegetation optical depth (VOD, τ) is a crucial parameter describing vegetation attenuation properties in the microwave radiative transfer equations (RTE) (Mo et al., 1982; Ulaby and Wilson, 1985). Although VOD was originally treated as a transition variable for correcting vegetation effects in SM retrieval algorithms, it has been proven to be a promising ecological indicator for studying plant hydraulics (Konings et al., 2019), carbon stocks (Fan et al., 2019; Fan et al., 2023; Liu et al., 2015), and vegetation phenology (Jones et al., 2011). Long-term and accurate global monitoring of SM and VOD are essential to enhance our knowledge on the linkage between water, and carbon cycles in terrestrial ecosystems.

Spaceborne passive microwave technology has experienced rapid development since the Skylab mission in the 1970s (Jackson et al., 2004). Current spaceborne microwave radiometers can be divided into two categories: (i) multi-frequency radiometers with selected channels from C-band (6.9 GHz) to W-band (89 GHz), and (ii) single-frequency radiometers at L-band (1.4 GHz). Although the L-band has been proven to be the optimal tool for monitoring SM, data of this band are only available for >10 years with the Soil Moisture and Ocean Salinity (SMOS) mission launched in November 2009 (Kerr et al., 2010) and the Soil Moisture Active and Passive (SMAP) launched in January 2015 (Entekhabi et al., 2010). On the other hand, multi-frequency radiometers at higher frequency bands provide a much longer heritage of measurements, although their sensitivity to SM is weaker than that of L-band. Among those multi-frequency radiometers, two typical spaceborne sensors are the Advanced Microwave Scanning Radiometer for Earth Observing System (AMSR-E) and its successor AMSR2. The AMSR-E was in orbit from 2002 to 2011 and carried on the National Aeronautics and Space Administration (NASA) satellite Aqua. It is a twelve-channel, six-frequency (from 6.9 to 89 GHz), total power passive-microwave radiometer system (Kawanishi et al., 2003). The AMSR2 launched aboard the Japan Aerospace Exploration Agency (JAXA) Global Change Observation Mission 1st-Water (GCOM-W1) satellite on May 18, 2012, is configured with instrument attributes (frequency band, incidence angle, etc.) similar to AMSR-E (Imaoka et al., 2012). In addition, AMSR3 is currently under development for launch in the future. The combined use of AMSR-E/2/3 brightness temperature (TB) observations could generate long-term data of SM and VOD, which are valuable for climate change studies.

Concurrent with the development of passive microwave spaceborne missions, the scientific community has also made large efforts for improving the retrieval methodology of SM and VOD at the global scale. Most SM and VOD retrievals designed for AMSR-E/2 are based on the tau-omega model (Mo et al., 1982), which is the zero-order solution of RTE by neglecting multiple scattering between vegetation and the surface. These retrieval algorithms could be grouped into three categories (Zhao et al., 2021):

(1) Algorithms based on the reverse-order RTE. Such algorithms usually only care about the accuracy of SM and require auxiliary data to compensate for vegetation and roughness effects. For example, the single channel algorithm (SCA, Jackson, 1993) implemented on AMSR-E adopted the historic averages of normalized difference vegetation index (NDVI) from the Advanced Very-High-Resolution Radiometer (AVHRR) for estimating the vegetation water content (VWC, equivalent to VOD) to reduce the unknowns. Although there was no public SCA-generated SM product from AMSR-E, this algorithm was tested to perform well over four experimental watershed sites (Jackson et al., 2010). It should be noted that the performance of such algorithms highly depends on the accuracy of auxiliary data and the calibrated model parameters related to vegetation and surface roughness.

(2) Iterative algorithms based on forward simulations of RTE. These algorithms usually use numerical solutions to estimate SM or VOD or both SM & VOD simultaneously by minimizing the cost function between forward TB simulations and observations. In the early stage of AMSR-E in-orbit, the multichannel iterative approach, which can simultaneously retrieve SM, VWC, and effective soil temperature, was chosen as the baseline algorithm (Njoku et al., 2003). However, RTE contains many nonlinear equations, and there are co-correlations in the observations. Iterative algorithms may generate multiple minima, which brings uncertainties to the final results. In this regard, researchers considered multi-temporal or multi-orbit observations to enhance the robustness of retrieval. The core assumption in multi-temporal or multi-orbit retrieval is that vegetation undergoes slower temporal changes than SM within a certain time window or several overpasses (Al Bitar et al., 2017; Konings et al., 2017; Wigneron et al., 2000). For example, Karthikeyan et al. (2019) retrieved the SM, VOD, and surface roughness simultaneously using the X-band AMSR-E observations, assuming that vegetation was invariant over seven days and roughness was constant throughout the year. Although the multi-temporal or multi-orbit strategies can reduce the retrieval noise, they may also mask the real change of vegetation after a rainstorm or severe drought. In addition to multi-parameter simultaneous retrieval, some studies use the observed or modeled SM as an input to retrieve VOD only. For example, Wang et al. (2021) combined the AMSR2 observations at X-band and SM from ERA5-land reanalysis data to retrieve VOD based on the forward simulations of X-band microwave emission of the biosphere (X-MEB).

(3) Algorithms based on microwave indices. These algorithms combine different channel information into appropriate indices and then establish their analytical relationship with geographic parameters. For example, the principle of the land parameter retrieval model (LPRM) is that VOD can be analytically derived from the microwave polarization difference index (MPDI) and soil emissivity (Meesters et al., 2005). LPRM was selected as the NASA operational algorithm for ASMR-E/2 to provide continuous SM and VOD data. However, many studies (Chen et al., 2013; Cui et al., 2017; Jackson et al., 2010) found that LPRM SM from ASMR-E/2 had a large positive bias when compared with in situ observations. It was indicated that LPRM is susceptible to errors correlated with MPDI, which measures the polarization difference between H-polarized and V-polarized TB. The value of MPDI may be low for small angular measurements, dry conditions, or dense vegetation, which makes LPRM lose sensitivity to SM (Van der Schalie et al., 2015; Zhao et al., 2020a). The standard algorithm from JAXA utilized the index of soil wetness (ISW) and polarization index (PI) to compile a lookup table and then estimate SM through the inverted lookup table (Fujii et al., 2009; Koike et al., 2004). Previous studies (Chen et al., 2017; Cui et al., 2017; Zheng et al., 2022) found that the JAXA SM from AMSR2 presented a relatively poor performance compared with network-based SM observations. Because the indices used in LPRM and JAXA contain information from both vegetation and soil, they can bring uncertainties to the SM retrievals. In this regard, the microwave vegetation indices (MVIs) were developed by Shi et al. (2008) to separate signals from soil and vegetation, and they were successfully utilized for AMSR-E SM estimation in the physically based statistical methodology proposed by Zhao et al.

(2011). However, the calculation of MVIs, the ratio of two highly correlated variables, requires high-quality data. Even if AMSR-E/2 observations are affected by weak radio frequency interference (RFI), which may lead to non-negligible uncertainties in MVIs, thus limiting its applications. It should be noted that the derivation of analytic relationships between microwave indices and geographic parameters is usually based on some assumptions (e.g., VOD and single scatter albedo should be the same for both polarizations in LPRM). Therefore, the uncertainty of such algorithms is directly affected by the model assumptions.

Although these algorithms could achieve good SM retrieval performance at the global scale or over some specific sites, most of them ignore or simplify the discrepancy of vegetation effects at different microwave frequencies, polarizations, and incidence angles. It is recognized that VOD varies at different microwave channels (hereafter the channel denotes incidence angle, polarization, and frequency), especially at the ground-based scale. Griend et al. (1996) showed that microwave transmissivity (the exponential equivalent of VOD) varies with incidence angles and indeed differs in both polarizations (V-polarized transmissivity is smaller than H-polarized) over a wheat field. Wigneron et al. (1995) developed an analytical formulation to relate VOD at different polarizations and angles and then achieved reliable SM retrievals over crop fields. Van de Griend and Wigneron (2004) performed a reanalysis for the vegetation attenuation coefficient b which relates VWC to VOD (VOD $= b \bullet$ VWC) and confirmed the b-factor is highly dependent on frequencies and canopy types. Ground-based radiometer observations in the Soil Moisture Experiment in the Luan River (SMELR, Zhao et al., 2020b) also indicated that b-factor at L band is not always the same for both different incidence angles and polarizations. However, in contrast to the ground-based experiments, researchers usually hypothesize that the polarization dependence of vegetation properties is weak at the satellite scale due to the large spatial heterogeneity of the satellite footprints. Moreover, most of the algorithms were implemented at a single band and it is difficult to estimate polarized VOD due to the lack of enough observations. Even when multi-frequency observations were used, they usually related VOD to a single VWC (Njoku and Li, 1999). Although ignoring the dependence of VOD on polarization or simplifying the frequency difference of VOD can reduce the unknowns to better serve the SM retrievals, these simplifications may lead to a risk of VOD retrieval, resulting in interpretation errors and failure to correctly understand VOD in plant physiology (Konings et al., 2021).

It is worth noting that there are few studies investigating the discrepancy of VOD in polarization and frequency at the satellite scale. Therefore, it is desirable and significant to design an algorithm that can estimate polarization- and frequency-based VOD while taking into account the accuracy of SM retrieval. In this context, this study adopted a multi-channel collaborative algorithm (MCCA) developed by Zhao et al. (2021) to tackle the above issues. The new algorithm comprehensively considers the physical relationship between multiple microwave channels and could retrieve SM and multi-channel VODs simultaneously. MCCA has been tested in ground-based radiometer measurements at corn and grass fields from the SMELR campaign and has shown good retrieval performance (Zhao et al., 2021). However, MCCA has not yet been implemented on satellite-based multi-frequency observations at the global scale.

It is a chance but also a challenge for us to explore the performance of MCCA at the global scale. In this study, we extended MCCA to the AMSR-E/2 configurations at the global scale. The main objectives of this study include: (1) to generate a long-term SM and VOD product using MCCA; (2) to compare the performance of MCCA SM and VOD with other products derived from or merged with AMSR-E/2 observations; and (3) to assess the dependence of VOD on polarization and frequency.

2. Datasets and methodology

2.1. Datasets

2.1.1. Brightness temperature from AMSR-E/2

In this study, multi-frequency gridded L3 TB products from AMSR-E/2 were used to retrieve SM and VOD. Considering that the contribution of the surface signal decreases with increasing frequency, this study only used the TB observations from AMSR-E/2 at 6.925, 10.65, 18.7 GHz for SM and VOD retrieval and 36.5 GHz at vertical polarization for effective temperature estimation (Holmes et al., 2009). To ensure the data consistency between the two sensors, we adopted a similar strategy as Yao et al. (2021) for TB inter-calibration. The only difference is that the TB reference used here is from AMSR-E instead of AMSR2. The harmonized multi-frequency TB data (2002−2021) was then used to generate long-term SM and VOD product.

2.1.2. In situ soil moisture for validation

To effectively validate the retrieved SM, ground-based measurements from 25 dense networks were used. These SM networks are from the International Soil Moisture Network (ISMN), the United States Department of Agriculture (USDA) watersheds, and the National Tibetan Plateau Data Center (TPDC). These SM networks cover a wide variety of climate regimes, land cover types, topography, and soil types around the world. Each network consists of multiple instrumented stations, and they have been proven to serve well in the calibration/validation activities of remotely-sensed SM retrievals (Colliander et al., 2017; Dorigo et al., 2011; Zheng et al., 2022). Details about each SM network are listed in Table A1 in Appendix A. It should be noted that sampling depth and representing depth was mismatched. Theoretically, the microwave remote sensing penetration depth varies across stations and time, and it is argued that topsoil moisture contributes the most to the microwave signal at C-, X- and Ku-bands. During the validation, we used the shallowest layers (most networks are <5 cm, except Adelong where it is 0–8 cm) as the reference and ignored the variation in penetration depth. This is a common practice used in many previous studies (Jackson et al., 2010; Ma et al., 2019; Zheng et al., 2022).

2.1.3. Vegetation datasets

Unlike SM, VOD is treated as a transition variable in RTE rather than an intuitive and easily measured parameter. It is challenging to implement a quantitative assessment of VOD. It is acknowledged that VOD is affected by water stress and is also sensitive to vegetation biomass. Many extant studies (Grant et al., 2016; Li et al., 2021) showed that VOD can generally capture similar seasonal cycles and interannual variations as NDVI. In this context, this study used aboveground biomass (AGB) and NDVI to indirectly evaluate the MCCA-derived VODs, the standard LPRM products from NASA (Richard de Jeu and Owe, 2011, 2014), and the VODCA product (Moesinger et al., 2020). The AGB map circa 2015 was produced from in situ inventory plots, spaceborne Lidar, and optical and microwave imagery through maximum entropy modeling (Saatchi et al., 2011). NDVI was extracted from MOD13C1 and MYD13C1 collection 6 (Didan, 2015a, 2015b) and combined to form the 8-day observations. In addition, pixels with snow/ice, clouds, estimated from historic time series, 'marginal' quality, non-processed, and non-land data were filtered before the analysis. To achieve uniform spatial resolution in the VOD assessment, both AGB and NDVI data were resampled to 0.25° by spatial averaging.

To be mentioned, in the absence of ground-truth VOD data, the spatial correlation between VOD and AGB and the temporal correlation between VOD and NDVI cannot be used as criteria for determining which VOD product performs better, but it can help to determine the similarities and differences between different VOD products. It is recognized that VOD could not simply be related to either water stress or biomass alone.

2.1.4. Other datasets

Soil texture, including the sand and clay fractions, was extracted from the regridded Harmonized World Soil Database (HWSD v1.2) for the usage in the soil dielectric model (Wieder et al., 2014). Since MCCA adopted the iterative calculation method, we extracted 11 years (2010−2020) of SM (level 1) from auxiliary files used for SMOS SM retrieval and made an average for the same day across all 11 years as the initial SM data. The initial SM data is the model output from the European Centre for Medium-Range Weather Forecasts (ECMWF). To be noted, the initial SM data is independent of satellite observations and used to initialize the iteration process rather than constraining the parameters in the cost function.

The land cover map for 2015 based on International Geosphere-Biosphere Programme (IGBP) schema was extracted from MCD12Q1 (Friedl and Sulla-Menashe, 2019) for the VOD comparison across different vegetation types. For the time series analysis of SM and VOD at selected sites or points, daily precipitation from the Integrated Multi-satellite Retrievals for Global Precipitation Measurement Final Precipitation Level 3 (GPM_3IMERGDF, version 06) (Huffman et al., 2019) was adopted in this study. To ensure a consistent spatial scale, all the above auxiliary data were aggregated to the 0.25° grid.

To further clarify the advantages of the proposed algorithm and retrieved SM, this study also made an inter-comparison with different SM products from AMSR-E/2 or reprocessed SM products, including the standard product from JAXA (Fujii et al., 2009; Koike et al., 2004), the official LPRM products from NASA (Owe et al., 2008; Richard de Jeu and Owe, 2011, 2014), the CCI passive merged SM product (CCI-P v07.1) from ESA (Dorigo et al., 2017; Gruber et al., 2019) and the artificial neural network (ANN) product by Yao et al. (2021).

2.2. Methodology

2.2.1. Multi-channel collaborative algorithm

Like most SM retrieval algorithms, MCCA is based on a zero-order approximation of RTE, known as the tau-omega model (Mo et al., 1982), which neglects multiple scattering effects within vegetation. Moreover, a two-component version for better separating the soil and vegetation contributions (Shi et al., 2008) was considered in MCCA, that is:

$$TB_{ch}^{measured} = V_{ch}^{e} + V_{ch}^{t} \bullet e_{ch}^{s} \tag{1}$$

where subscript *ch* represents different channels, hereafter used to indicate the polarization (*P*), incidence angle (θ), and frequency (f); superscript *s* denotes rough soil surface; $TB_{ch}^{measured}$ is the total brightness temperature measured at channel *ch*; e_{ch}^{s} represents the emissivity coming from the rough soil surface, which is a function of the soil dielectric constant ϵ_{ch}^{s} and the surface roughness *Rou*; V_{ch}^{e} is the vegetation emission term; V_{ch}^{t} is the vegetation transmission term. V_{ch}^{e} and V_{ch}^{t} are described as follows:

$$V_{ch}^{e} = \left[F^{v} \bullet e_{ch}^{v} \bullet (1+\Gamma_{ch})\right] \bullet T^{v} \tag{2}$$

$$V_{ch}^{t} = \left[(1-F^{v}) + F^{v} \bullet \Gamma_{ch}\right] \bullet T^{s} - \left(F^{v} \bullet \Gamma_{ch} \bullet e_{ch}^{v}\right) \bullet T^{v} \tag{3}$$

where F^{v} is the vegetation coverage within the radiometer footprint; e_{ch}^{v} is the vegetation emissivity, given by the equation $e_{ch}^{v} = (1-\omega_{ch}) \bullet (1-\Gamma_{ch})$. In this equation, ω_{ch} is the vegetation single scatter albedo, and Γ_{ch} is the transmissivity denoting the one-way attenuation effect of vegetation. T^{v} and T^{s} represent effective vegetation and soil temperature, respectively, which are considered to be approximately equal by assuming the vegetation and soil are in thermal equilibrium.

When there is more than one channel of observations, the relationship (abbreviated as F_{cond}) between any two channels without any assumptions can be expressed as follows (Zhao et al., 2021):

$$F_{cond}: TB_{ch(2)}^{measured} = V_{ch(2)}^{e} - S_r V_r \bullet V_{ch(1)}^{e} + S_r V_r \bullet TB_{ch(1)}^{measured} \tag{4}$$

where $S_r = \frac{e_{ch(2)}^{s}}{e_{ch(1)}^{s}}$ is the ratio of soil emissivity as a function of SM and surface roughness *Rou*; and $V_r = \frac{V_{ch(2)}^{t}}{V_{ch(1)}^{t}}$ is the ratio of vegetation transmission terms. Eq. (4) implies that when the brightness temperature and corresponding soil and vegetation parameters at one channel are known, the brightness temperature at another channel can be predicted. Eq. (4) is a key conditional restriction in MCCA as it relates to the information of all available channels.

SM and surface roughness are considered to be independent of microwave observations. In contrast, MCCA treats effective single scatter albedo (ω) and VOD as variables that depend on polarization, incidence angle, and frequency. When multi-channel information is provided, the unknown parameters increase to include $\{SM, Rou, \omega_{ch(1)}, \tau_{ch(1)}, \omega_{ch(2)}, \tau_{ch(2)}, \ldots, \omega_{ch(N)}, \tau_{ch(N)}\}$. This is an ill-posed problem as there are more unknowns than observations. To reduce the number of unknowns, Zhao et al. (2021) proposed a general VOD relationship (abbreviated as F_{asm}) between any two channels based on previous studies (Jackson and Schmugge, 1991; Wigneron et al., 1995):

$$F_{asm}: \frac{\tau_{ch(2)}}{\tau_{ch(1)}} = \left(\frac{f_2}{f_1}\right)^{C_f} \bullet \frac{sin^2\theta_2 \bullet C_{P2} + cos^2\theta_2}{sin^2\theta_1 \bullet C_{P1} + cos^2\theta_1} \tag{5}$$

where $C_f > 0$ and $C_P > 0$ are parameters characterizing the dependence of τ_{ch} on frequency and polarization, respectively, and should depend on vegetation types.

For a given brightness temperature at a certain channel ($TB_{ch}^{measured}$) with corresponding known variables, $\{e_{ch}^{s}, \omega_{ch}, F^{v}, T^{v}, T^{s}\}$, a VOD value can be derived based on the reverted tau-omega model. As proposed by Zhao et al. (2021), vegetation transmissivity (Γ_{ch}) can become the only unknown in a quadratic equation after rearranging the tau-omega model. Thus, vegetation transmissivity can be analytically derived as follow:

$$\Gamma_{ch}^{-} = \frac{-b' - \sqrt{b'^2 - 4 \bullet a' \bullet c'}}{2 \bullet a'} \tag{6}$$

or another solution:

$$\Gamma_{ch}^{+} = \frac{-b' + \sqrt{b'^2 - 4 \bullet a' \bullet c'}}{2 \bullet a'} \tag{7}$$

The superscript "-" or "+" represents the root of a quadratic equation with subtraction or addition, respectively. Considering the definition of vegetation transmissivity in nature, only the value of Γ_{ch} between 0 and 1 is valid. For the dual polarization configuration, whether to use Eq. (6) or Eq. (7) at a certain frequency band depends on the criterion that the vegetation transmissivity at horizontal polarization should be close to that at vertical polarization. The coefficients $\{a', b', c'\}$ are defined as:

$$a' = -\left(1 - e_{ch}^{s}\right) \bullet (1-\omega_{ch}) \bullet T^{v} \tag{8}$$

$$b' = e_{ch}^{s} \bullet \left[T^{s} - (1-\omega_{ch}) \bullet T^{v}\right] \tag{9}$$

$$c' = (1-\omega_{ch}) \bullet T^{v} - TB_{ch}^{v} \tag{10}$$

where TB_{ch}^{v} is the brightness temperature emitted from vegetated areas:

$$TB_{ch}^{v} = \frac{TB_{ch}^{measured} - (1-F^{v}) \bullet e_{ch}^{s} \bullet T^{s}}{F^{v}} \tag{11}$$

After vegetation transmissivity is solved, VOD can be derived by the following formula:

$$VOD_{ch} = -ln(\Gamma_{ch}) \bullet cos\theta_{ch} \tag{12}$$

In particular, parameters C_f and C_P are only related to the vegetation types and independent of microwave observations. If these two parameters can be given or calibrated, the retrieval unknowns will be reduced. For the AMSR configuration in this study, vegetation single scatter albedo (ω) was further assumed to depend only on frequency, and vegetation cover fraction was set as 1 to facilitate the MCCA retrieval. Thus, there are five unknowns $\{SM, Rou, \omega_{06}, \omega_{10}, \omega_{18}\}$, where the subscript "06", "10", and "18" denotes the frequency of C-, X-, and Ku-bands, respectively, and VOD can be derived from the reverted tau-omega model. According to the aforementioned description, the retrieval procedure of MCCA can be carried out in the iterative form as follows:

(i) estimating the initial values of $\{SM^0, Rou^0, \omega_{06}^0, \omega_{10}^0, \omega_{18}^0\}$ and then selecting a core channel and calculating the corresponding VOD from Eq. (6), Eq. (7), and Eq. (12). As for this study, H-polarization at 10.65 GHz (10H) was set as the core channel based on the following factors: (1) X-band is less susceptible to RFI than C-band at global scale and has the stronger penetration ability than Ku-band (Njoku et al., 2005). (2) H-polarization at X-band is more sensitive to SM than the V-polarization (Mladenova et al., 2014). Based on the assumed relationship between VODs at different channels (Eq. (5)), the VOD at collaborative channels can be estimated when the parameters C_f and C_P are known.

(ii) with the input parameters $\left\{SM^0, Rou^0, \omega_{06}^0, \omega_{10}^0, \omega_{18}^0, \tau_{ch(2:N)}^0\right\}$, the TB at collaborative channels can be calculated with the F_{cond} of Eq. (4).

(iii) establishing the cost function between observed and simulated TB at collaborative channels and repeating the iterative process. When the cost function approaches the minimum, the parameters $\{SM, Rou, \omega_{06}, \omega_{10}, \omega_{18}\}$ can be determined and then VOD at different channels can be estimated from Eq. (6), Eq. (7), and Eq. (12). The cost function is as follows:

$$min\Phi(X) = \sum_{i=2}^{N} W_i \bullet \frac{\left(TB_{ch(i)}^{estimate} - TB_{ch(i)}^{measured}\right)^2}{\sigma\left(TB_{ch(i)}\right)} \tag{13}$$

where i is the index of the auxiliary channel, N is the total number of channels, $TB_{ch(i)}^{estimate}$ is the simulated TB from Eq. (4), and $TB_{ch(i)}^{measured}$ is the observed TB at collaborative channels. W_i is the weight describing the contributions from different collaborative channels and was set to 1 here. $\sigma\left(TB_{ch(i)}\right)$ is the measurement noise at each channel and was set to 1 K.

In this study, only six channels (10H, 10V, 06H, 06V, 18H, 18V) from AMSR-E/2 were used in MCCA, and one of them (the 10H core channel) was used as a constraint. To make the retrievals possible, the parameters C_f and C_P should be known. Thus, the number of correlated observations is equal to the number of unknowns ($\{SM, Rou, \omega_{06}, \omega_{10}, \omega_{18}\}$). Parameter C_f was determined by model selection as described later, and parameter C_P was set as 1, which is a commonly used assumption in previous studies (Fernandez-Moran et al., 2017; Wigneron et al., 2017). It is worth noting that setting the parameter C_P to 1 does not prevent retrieving the VOD at both H- and V-polarizations, because the parameters $\{SM, Rou, \omega_{06}, \omega_{10}, \omega_{18}\}$ were firstly obtained and then the final VOD was estimated from Eq. (6), Eq. (7), and Eq. (12).

To be mentioned, there are two differences between MCCA and other algorithms implemented on AMSR. First, MCCA is a multi-channel (frequency and polarization) retrieval method, while other algorithms like LPRM or X-MEB were performed on independent retrievals at different frequencies. Second, it is assumed in MCCA that VOD varies with polarization while SM is independent of polarization, which is opposite to SCA. This assumption in MCCA is more in line with physical reality, because SM is a state variable of soil independent of polarization, while VOD accounts for the microwave attenuation through vegetation and should be susceptible to polarization.

For the implementation of MCCA, the effective soil temperature was estimated using the Ka-band (37 GHz) observations according to the method of Holmes et al. (2009). For the daytime (ascending) observations, the following equation is used:

$$T^s = 0.898 \bullet TB_{37V} + 44.2 \tag{14}$$

for the nighttime (descending):

$$T^s = 0.893 \bullet TB_{37V} + 44.8 \tag{15}$$

To account for the surface roughness effect, we used the Qp model proposed by Shi et al. (2005) in this study. It is a parameterized multi-frequency polarization surface emission model and has been proven to perform well in the AMSR configuration (Shi et al., 2005). In this study, we further adopted the parametric scheme of the Qp model, because it can be simply described as a single-surface roughness property—the ratio of the surface root mean squared height (s) and the correlation length (l). The Mironov model has been widely applied for SM retrieval with the SMOS and SMAP missions (Mironov et al., 2004), and here was also utilized for calculating soil dielectric constants under different soil moisture content.

2.2.2. Parameter tuning

Although multi-channel information is provided in AMSR, there should be fewer unknowns than observations. When MCCA was implemented on AMSR-E/2, we made two simplifications: (i) vegetation single scatter albedo is only dependent on microwave frequency; (ii) parameters C_f and C_P were calibrated before the retrievals. With these two assumptions, the equivalent five observations are equal to the five equivalent unknowns ($\{SM, Rou, \omega_{06}, \omega_{10}, \omega_{18}\}$), and then the retrieval can be carried out. Furtherly, parameter C_f is the main concern of this study. In this study, we assumed that C_f is constant with time and only varies with locations/pixels. Therefore, the parameter C_f was determined per-pixel through a model selection, that is, the optimal C_f leads to the minimum sum of the cost function:

$$\min_{C_f} J = \sum_{j=1}^{M}\left[min\Phi(X) = \sum_{i=2}^{N} W_i \bullet \frac{\left(TB_{ch(i)}^{estimate} - TB_{ch(i)}^{measured}\right)^2}{\sigma\left(TB_{ch(i)}\right)}\right] \tag{16}$$

where M is the number of observations. The external optimization process is similar to one of the previous studies (Feldman et al., 2018; Konings et al., 2017). For the global study, a full year of data from AMSR-E descending orbit in 2010 was selected for tuning parameters. Considering the computational tractability, C_f was set from 0 to 1.5 with an increment of 0.1 (it has been tested that the interval <0.1 makes little effect on the final inversion results). The global map of C_f is shown in Fig. B1 in Appendix B, and the result exhibited different ranges of C_f with different vegetation types. It should be pointed out that C_f serves as a parameter for the retrieval in this study, and there is no measured or published data for its verification.

2.2.3. Evaluation method

In this study, SM and VOD are the variables we focus on in MCCA inversion results. For each dense SM network, a rectangular boundary was defined by the maximum and minimum latitude and longitude of the stations within the network. The arithmetic mean of all stations in the SM network was taken as the ground truth, and the retrieved SM of the grid cells (0.25° or EASE2) located within the rectangular boundary were averaged and compared with the ground truth. Up-scaling the station observation is much more complex since SM heterogeneity is driven by many factors (precipitation distribution, topography, soil texture and land cover). Although arithmetic averaging is not an optimal way to reduce the effects of spatial heterogeneity, it is the most direct method to ensure that all SM networks are evaluated under the same criterion. In addition, the period used for the SM validation was aligned with the available period when all six satellite-based and in-situ SM data are available at the same time from 2002 to 2021. Four classical

statistical metrics were used to evaluate the six SM products, including Pearson's correlation coefficient (R), root mean square error (RMSE), mean bias and the unbiased root mean square error (ubRMSE). Because the time interval of each SM network measurement varied from 10 min to 60 min, we consistently used the in-situ observations at the local time of 2:00 to perform the validation. Evaluation was not performed on the ascending data since the ANN only provided SM in descending orbit. To ensure the fairness of the inter-comparison, these SM products corresponding to the network were filtered by their quality control (QC) file, and the statistical metrics calculation was only conducted in the intersection of all data.

We randomly selected three full years of data (2014–2016) for the

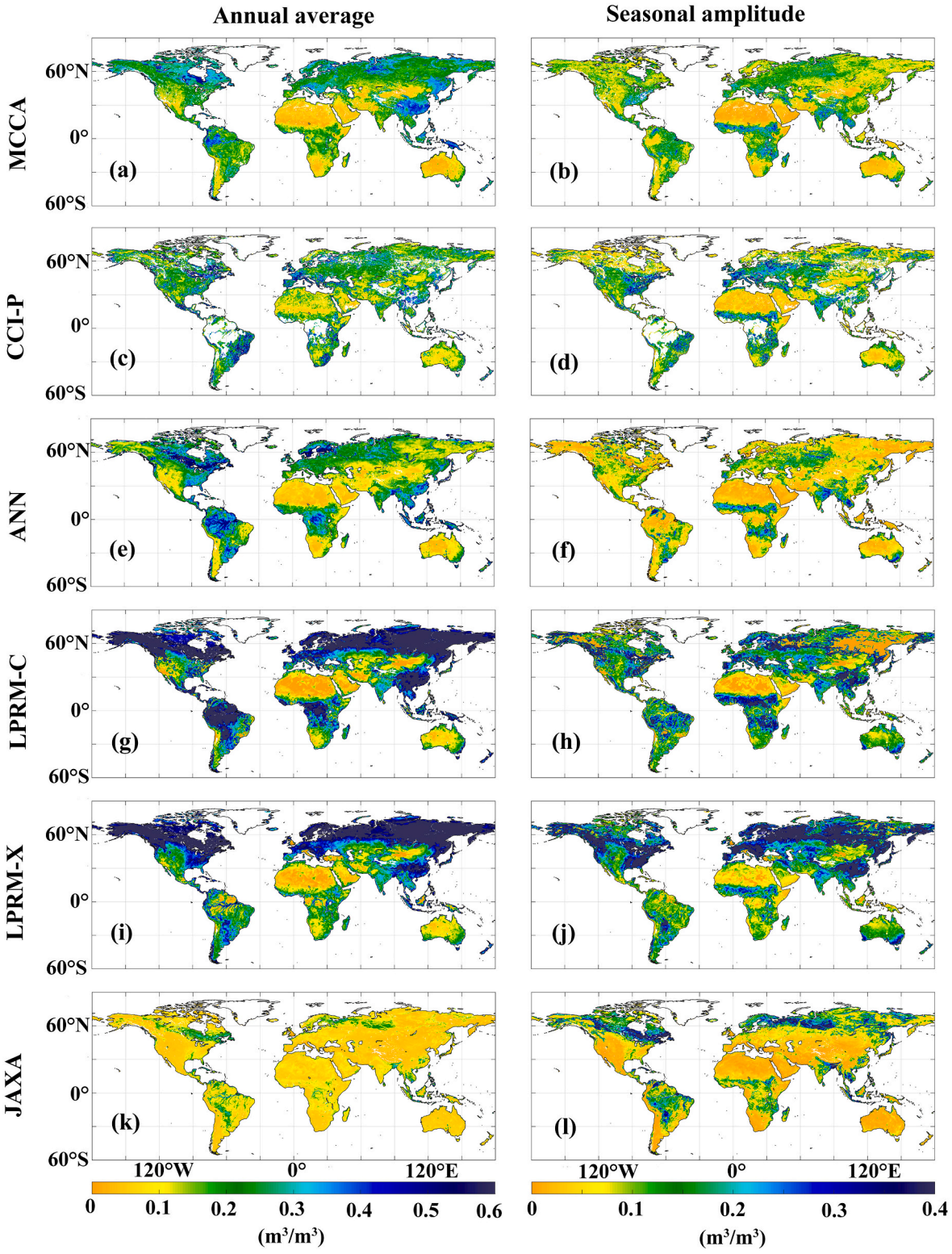

Fig. 1. Annual means and seasonal amplitudes of soil moisture averaged over the period from 2014 to 2016. (a-b) MCCA. (c-d) CCI-passive. (e-f) ANN. (g-h) LPRM-C. (i-j) LPRM-X. (k-l) JAXA.

spatial analysis among different SM and VOD products. Poor data were removed according to the following criteria: (1) values <0; (2) values over frozen land surface; (3) values affected by RFI; (4) values beyond the IQR range. In addition, pixels with an effective number of values lower than 30 for one year were discarded.

When the VOD was indirectly evaluated with AGB and NDVI, strict data processes should be carried out further. To reduce the effect of water stress, we averaged data from descending and ascending orbits to daily values after filtering based on the aforementioned criteria. Because the AGB used here is a static map circa 2015, the annual averaged VOD from 2014 to 2016 was calculated for the comparison. For the temporal consistent comparison with NDVI for three years (2014–2016), daily VOD was averaged per pixel to give 16-day mean values, which were produced every 8 days (Grant et al., 2016). For example, 'day 001' includes acquisitions between days 1 and 16, 'day 009' includes acquisitions between days 9 and 24, etc. In addition, pixels with the summed fraction of urban, wetland, open water, and ice >10% were masked.

3. Results

3.1. Performance of SM retrievals

3.1.1. Spatial patterns of SM

The global spatial pattern of six SM products (MCCA, CCI-P, ANN, LPRM-C, LPRM-X, and JAXA) is shown in Fig. 1. The left column is the annual average of SM, and the right column represents the seasonal amplitude of SM. Seasonal amplitude (SA) is defined as the difference between 95% and 5% percentile of the data after smoothing using a 45-day sliding average window (Konings et al., 2017). The mean and seasonal amplitude of SM were calculated from the annual averages over three years (2014–2016).

In general, MCCA shows similar spatial patterns of SM as ANN, which is fed with the SMAP SM product, with the lowest SM values in desert regions (e.g., the Sahara of Africa, desert areas in central Asia, and the Taklamakan in the northwest of China) and relatively high SM values in dense forests (e.g., boreal forest areas, Amazon, the southeast of Asian, and southeast of China). CCI-P has slightly larger SM values than MCCA and ANN in the above dry areas and also shows high values in the boreal forest region. Because a mask for rainforest was applied in the merging process for CCI-P, there are some blank areas near the equator in Fig. 1 (c-d). The spatial features of LPRM-C are very close to those of LPRM-X in most regions, and they present higher SM values on the whole. In comparison with MCCA, LPRM-C and LPRM-X produced much higher SM values in boreal forest areas (exceeding 0.6 m^3/m^3) and smaller or the same SM values in the Sahara. JAXA presents very low SM values over most of the globe, except northern Russia, northeastern Canada, and southwestern Brazil. As to the SM variation across different regions, MCCA and ANN show a distinct dry-wet gradient in the north-south direction of Africa and the west-east direction of the continental United States. Regarding the absolute SM values, there are irregular differences among MCCA, CCI-P, and ANN. In northeastern Canada, ANN shows the highest SM values, followed by MCCA and CCI-P. In southeastern China, MCCA has the largest SM values, followed by ANN and CCI-P. In eastern Brazil, the descending order of SM values is CCI-P, MCCA, and ANN. In Australia, MCCA is very similar to ANN, and is lower than CCI-P. The rank order of the magnitudes is not consistent.

The right column of Fig. 1 clearly shows the seasonal variation of SM, with similarities but also differences among the six products. Overall, LPRM-C and LPRM-X have the largest magnitude of seasonal variations, and MCCA is comparable to CCI-P in the seasonal amplitude of SM. In addition, the seasonal amplitudes of ANN and JAXA are smaller than that of MCCA over most regions. Regarding the distribution of seasonal cycles, analogous spatial patterns can generally be found in Fig. 1(b, d, f, h, j, l). For example, all datasets have relatively high values of seasonal amplitude in the Indian Peninsula, Indochina, the Sahel region, and the Miombo woodlands, which are significantly affected by the monsoon precipitation. On the other hand, the seasonal amplitude of MCCA in eastern Siberia is lower than that in western Siberia, which is similar to those of CCI-P, ANN, and LPRM-C, while LPRM-X and JAXA show little difference in seasonal amplitude of SM between the eastern and western Siberia. In the eastern United States, all the SM products except JAXA exhibit seasonal changes, and LPRM-X has the highest amplitude values of SM followed by LPRM-C, CCI-P, MCCA, and ANN. JAXA also fails to capture the seasonal changes of SM in Australia while the other five SM products can. In addition, the seasonal amplitude of MCCA in Australia is very similar to that of ANN, and LPRM-C/X and CCI-P show larger seasonal fluctuations than MCCA in Australia.

3.1.2. Validation and inter-comparison of SM products

The validation statistics of six SM products are shown in Table 1, and the RMSE values are shown in Table A2 in Appendix A. In terms of the correlation with in situ observations, each SM product has a wide range of R values among various networks. For the MCCA-derived SM, R values vary from 0.139 (SMN-SDR network) to 0.892 (Benin network). The R-value of CCI-P reaches the minimum (0.230) at the Manitoba network and the maximum (0.861) at the Benin network, while the ANN reaches the minimum (0.102) at the Adelong network and the maximum (0.844) at the REMEDHUS network. For the standard SM products from NASA and JAXA, the R range is 0.082–0.883 for LPRM-C, 0.164–0.867 for LPRM-X, and 0.100–0.806 for JAXA, respectively. Generally, MCCA produced higher values of R than JAXA except for the Manitoba, Walnut Gulch, and Maqu networks. On the other hand, MCCA shows similar performances with LPRM-C/X and is comparable to ANN in terms of R. The ANN SM is based on pixel-wise neural network training from the SMAP L3 SCA-V products, and it can be considered as a proxy of SMAP SM. Thus, this may be a reason explaining why ANN shows larger R values than MCCA in Walnut Gulch, Little Washita, Fort Cobb, and Little River networks. CCI-P obtains the highest R values over most of networks (16 over 25). Because CCI-P is a merged product that combines multiple passive microwave missions including SMOS and SMAP, and microwave observations at L-band are superior to C-, X-, and Ku-bands in capturing the temporal variation of SM. The better R performances of CCI-P over individual networks may be related to the weighted merging strategy in the reprocessing.

Regarding ubRMSE, MCCA has the narrowest range among different networks than other five SM products. As shown in Table 1, the ranges of ubRMSE from MCCA, CCI-P, ANN, LPRM-C, LPRM-X, and JAXA are 0.028–0.068 m^3/m^3, 0.034–0.082 m^3/m^3, 0.026–0.136 m^3/m^3, 0.035–0.117 m^3/m^3, 0.035–0.140 m^3/m^3, 0.024–0.121 m^3/m^3, respectively. In addition, MCCA presents the lowest ubRMSE values over 9 networks, same as ANN and 2 more than CCI-P. For the NASA standard products, both LPRM-C and LPRM-X produce relatively larger ubRMSE values than MCCA over most networks (24 over 25). MCCA also outperforms JAXA in terms of ubRMSE for most networks (17 over 25).

The bias ranges of MCCA, CCI-P, ANN, LPRM-C/X, and JAXA are −0.101-0.112 m^3/m^3, −0.103-0.226 m^3/m^3, −0.060-0.217 m^3/m^3, −0.005-0.340 m^3/m^3, 0.040–0.348 m^3/m^3, −0.259-0.049 m^3/m^3, respectively. In total, ANN obtains the bias close to zero over 9 networks, followed by MCCA over 6 networks and LPRM-C over 4 networks. Overall, both LPRM-C and LPRM-X show relatively large positive biases on most networks, while JAXA shows sizeable negative biases.

Because some stations of FMI, HOBE, Adelong, Kyemba, Yanco, REMEDHUS, TERENO, UDC-SMOS, Walnut Gulch, Fort Cobb, Little River and Pali networks were located on different land cover types (relabeled by the MODIS IGBP map), the weighted average SM based on the fraction of land cover was also adopted to validate the SM products. As shown in Fig. B2 in Appendix B, only TERENO and Walnut Gulch networks show a slight improvement in the validation among all six SM products. As for other SM networks, the differences in error metrics between the two kinds of validation have both positive and negative values. Overall, these differences in error metrics are small in magnitude, indicating that the validation using the arithmetic average SM is

Table 1
The network-based statistical validation results of six SM products. The best performance of the six SM products in each network is typeset in boldface.

Network	No.	R ($p < 0.05$)						ubRMSE (m^3/m^3)						Bias (m^3/m^3)					
		MCCA	CCI-P	ANN	LPRM-C	LPRM-X	JAXA	MCCA	CCI-P	ANN	LPRM-C	LPRM-X	JAXA	MCCA	CCI-P	ANN	LPRM-C	LPRM-X	JAXA
Benin	1415	**0.892**	0.861	0.822	0.843	0.798	0.618	**0.057**	0.073	**0.057**	0.076	0.069	0.058	0.056	0.226	0.107	0.067	0.040	**−0.027**
Niger	1042	0.833	0.620	0.802	**0.883**	0.867	0.806	0.028	0.039	**0.026**	0.035	0.035	0.036	**0.014**	0.121	0.022	0.017	0.040	0.049
FMI	690	0.187	**0.332**	0.279	0.211	0.214	0.100	**0.033**	0.041	0.040	0.098	0.091	0.093	**−0.017**	0.031	0.113	0.340	0.348	0.040
HOBE	2034	0.483	**0.664**	0.555	0.082	0.547	0.351	**0.044**	0.045	0.046	0.080	0.066	0.107	0.062	−0.023	**0.017**	0.247	0.223	−0.024
Adelong	633	0.799	0.846	0.102	**0.871**	0.810	0.608	0.052	**0.050**	0.136	0.099	0.110	0.067	−0.048	**0.015**	0.217	0.126	0.040	−0.059
Kyemba	2442	0.697	**0.794**	0.749	0.731	0.771	0.527	0.062	**0.056**	0.078	0.080	0.090	0.074	−0.042	0.069	0.068	**0.020**	0.062	−0.057
Yanco	3015	0.736	**0.853**	0.807	0.785	0.775	0.534	0.049	**0.038**	0.059	0.057	0.064	0.062	**−0.024**	0.058	0.047	0.053	0.075	−0.047
REMEDHUS	3552	0.805	**0.857**	0.844	0.826	0.819	0.608	0.046	0.064	**0.037**	0.091	0.114	**0.037**	0.011	0.121	**0.007**	0.135	0.106	−0.062
Manitoba	678	0.150	0.230	**0.425**	0.176	0.164	0.373	**0.059**	0.074	0.067	0.109	0.129	0.089	**−0.006**	0.010	−0.031	0.123	0.165	−0.127
Ontario	558	0.421	**0.485**	0.325	0.344	0.385	0.223	0.062	0.072	**0.060**	0.114	0.140	0.107	−0.086	0.010	**−0.006**	0.126	0.199	−0.181
Saskatchewan	696	0.670	**0.800**	0.759	0.294	0.500	0.280	0.048	**0.039**	0.042	0.101	0.091	0.068	0.054	0.080	**0.027**	0.219	0.256	−0.088
TERENO	2127	0.613	**0.704**	0.686	0.582	0.635	0.301	0.065	**0.056**	0.057	0.069	0.090	0.091	**0.011**	0.075	0.036	0.076	0.204	−0.117
UDC-SMOS	905	0.353	**0.477**	0.301	0.466	0.473	0.211	**0.053**	0.065	0.056	0.087	0.123	0.081	**−0.048**	−0.080	−0.060	0.160	0.174	−0.212
Walnut Gulch	4417	0.512	**0.712**	0.657	0.624	0.509	0.592	0.039	0.054	**0.027**	0.061	0.081	0.028	0.062	0.205	0.045	0.052	0.140	**−0.014**
Little Washita	2230	0.526	0.670	**0.736**	0.647	0.505	0.392	0.063	0.051	**0.041**	0.074	0.097	0.054	−0.030	−0.012	0.011	**0.003**	0.113	−0.096
Fort Cobb	2036	0.511	0.679	**0.700**	0.651	0.537	0.471	0.051	0.047	**0.043**	0.060	0.082	0.050	−0.101	−0.023	−0.017	**0.002**	0.090	−0.099
Little River	3793	0.650	0.735	**0.751**	0.567	0.595	0.347	0.046	**0.037**	0.039	0.069	0.084	0.071	0.078	0.052	0.116	0.168	0.200	**0.020**
St Josephs	1381	0.634	**0.699**	0.522	0.575	0.544	0.170	**0.057**	0.060	0.068	0.079	0.115	0.099	−0.053	−0.056	**−0.006**	0.014	0.162	−0.154
South Fork	1011	0.550	**0.596**	0.544	0.503	0.487	0.345	**0.063**	0.082	**0.063**	0.117	0.138	0.087	−0.072	**−0.003**	−0.059	0.028	0.115	−0.173
Reynolds Creek	2178	0.671	0.648	0.614	0.691	**0.730**	0.524	**0.048**	0.058	0.051	0.082	0.082	0.057	0.013	0.050	0.011	**−0.005**	0.092	−0.062
Maqu	1258	0.302	**0.353**	0.302	0.349	0.335	0.326	0.068	0.082	0.089	0.087	0.089	**0.066**	0.041	−0.103	**−0.002**	0.109	0.073	−0.259
Naqu	862	0.678	**0.800**	0.687	0.762	0.771	0.598	**0.060**	0.063	0.066	0.065	0.070	0.121	0.024	0.023	**0.004**	0.122	0.159	−0.051
Pali	344	0.532	**0.623**	0.587	0.538	0.598	0.464	0.038	0.040	**0.030**	0.060	0.062	0.033	0.112	−0.026	**−0.024**	0.129	0.177	−0.107
Shiquanhe	197	0.626	0.625	0.608	**0.653**	0.643	0.543	0.051	0.034	0.026	0.051	0.051	**0.024**	0.019	0.080	**−0.014**	0.110	0.154	−0.071
SMN-SDR	443	0.139	**0.454**	0.180	0.261	0.223	0.110	0.065	**0.040**	0.051	0.061	0.067	0.044	−0.030	**−0.015**	−0.058	0.054	0.072	−0.106
Overall	39,937	0.709	0.446	0.704	0.711	**0.735**	0.397	**0.073**	0.100	0.074	0.109	0.111	0.096	**0.007**	0.058	0.033	0.087	0.132	−0.066

relatively reasonable.

Fig. 2 shows the comparison of different SM products with in situ observation over all networks. Although the R-value of MCCA (0.709) is slightly lower than that of LPRM-C (0.711) and LPRM-X (0.735), it has the best performance in terms of RMSE (0.074 m^3/m^3), ubRMSE (0.073 m^3/m^3) and bias (0.007 m^3/m^3). ANN shows slightly lower performance than MCCA with the R value of 0.704, RMSE value of 0.081 m^3/m^3, ubRMSE value of 0.074 m^3/m^3, and bias value of 0.033 m^3/m^3. LPRM-C shows a similar pattern to LPRM-X, and they have large overestimations in the total scatter plot. On the contrary, JAXA exhibits a slightly weak correlation and has a sizeable underestimation. It should be pointed out that the R value of CCI-P is not high in the overall comparison, which is caused by lower covariance between the CCI-P and in situ SM over all networks. When the SM is <0.2 m^3/m^3, there is an overestimation in CCI-P. This is similar to the LPRM products in that they are derived from the same algorithm but with different versions.

To visualize the performance of each product, five networks from different continents (Benin in Africa, Yanco in Oceania, TERENO in Europe, Reynolds Creek in America, and Naqu in Asia) were selected for the time series of analysis. As presented in Fig. B3-B7 in Appendix B, MCCA shows good consistency with the in situ SM for all these networks. Like other SM products, MCCA can track well the temporal variations of SM caused by rainfall, irrigation, and surface thawing and can also capture well the dry-down of soil.

3.2. Performance of VOD retrievals

3.2.1. Spatial patterns of VOD

MCCA retrieved VODs were inter-compared with the LPRM products and the VODCA products based on the data from 2014 to 2016. The annual averages and seasonal amplitudes of VODs were calculated in the same way as SM, and their spatial patterns are shown in Fig. 3. All the VOD products have similar spatial distributions with the lowest values in semi-arid areas and the highest values in tropical forests. In general, the magnitude of VOD increases with frequency, which is more obvious in the MCCA products. The annual averages of VOD from different products are different, even for the VOD at the same band. VOD at Ku-band from MCCA shows the highest values (about 1.7–1.8) in the densely vegetated regions while VOD at C-band from VODCA presents the lowest values (nearly 0.6). Although all the VOD products exhibit different magnitudes in absolute values, they are still comparable to each other in terms of spatial gradients over the globe. For example, VODs increase significantly and synchronously with the vegetation density from northwest to southeast China. It is worth noting that most VOD gradient variations are consistent with the dry-wet changes of SM or climates.

Regarding the seasonal amplitude, some similar spatial features can still be found among different VOD products. The Sahel region and Miombo woodlands, which are affected by the tropical monsoon, show strong seasonal cycles of VOD. In regions including western Russia, the Indian Peninsula, the northeastern United States, and the southeastern coastal zone of Australia, VODs also exhibit distinct seasonality. Overall, VOD at Ku-band from MCCA has the highest values of seasonal amplitude. The V-polarized VODs from MCCA are slightly larger than the H-polarized VODs. In addition, MCCA-derived VODs have larger magnitudes than the other VOD products at C-, or X-, or Ku-bands. Interestingly, both polarized VODs at Ku-band from MCCA present some seasonal variations around the river streams in Amazon and Congo rainforest regions. It is recognized that the penetration ability of Ku-band is the weakest compared with the C- and X-bands, so the observation at Ku-band is susceptible to the surface canopy water (rain interception and dew formation). This phenomenon does not appear in the Ku-band of VODCA, which may be related to the processing method for VODCA products. According to the description of Moesinger et al. (2020), the Cumulative distribution function (CDF) matching technique was applied to scale outliers and the arithmetic mean between temporally overlapping observations was taken for aggregating the data. This fusion method may remove some physical variations, possibly caused by surface canopy stored water.

Boxplots of the average from MCCA VOD per land cover types shows that barren and sparsely vegetated areas have the lowest VOD values on

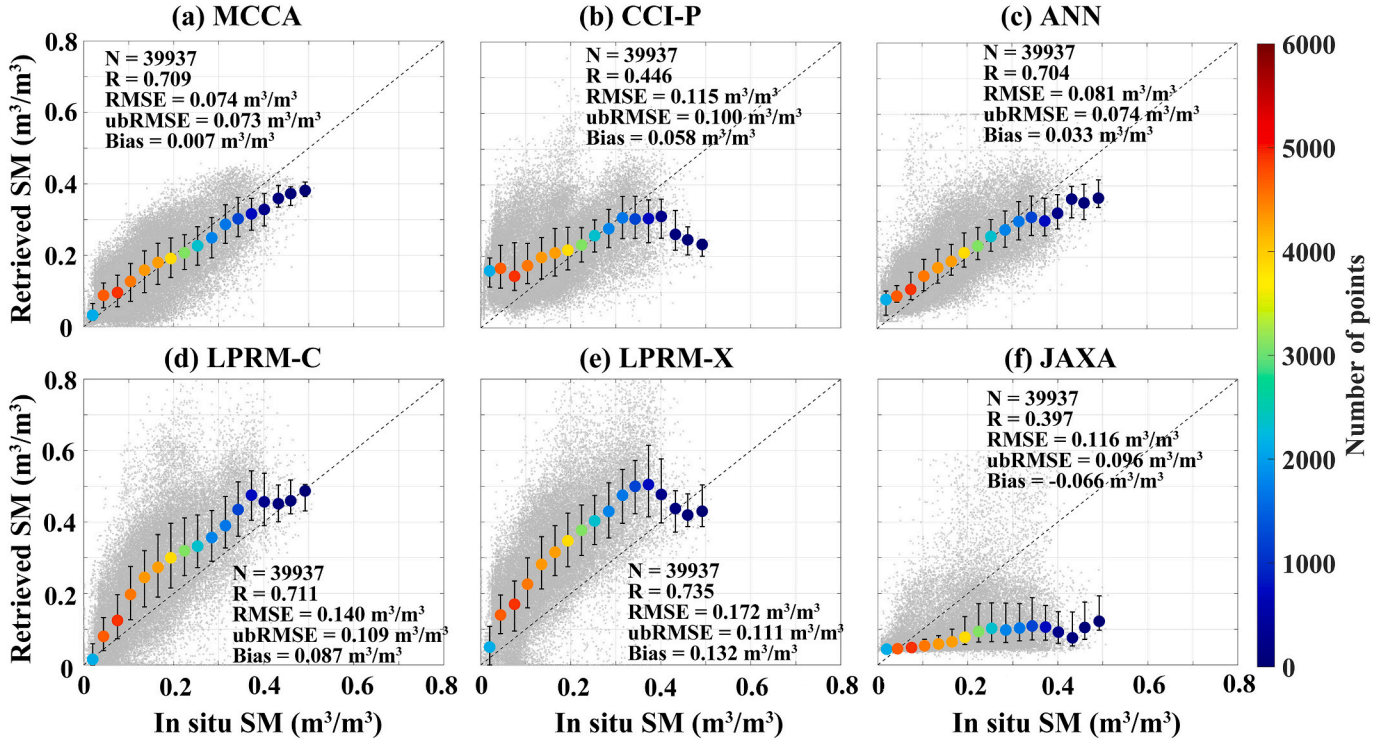

Fig. 2. Total soil moisture scatter with in situ observations. (a) MCCA (b) CCI-passive (c) ANN (d) LPRM-C (e) LPRM-X (f) JAXA. Circles and bars represent the median and inter-quartile ranges of SM for 0.03 m^3/m^3 wide bins.

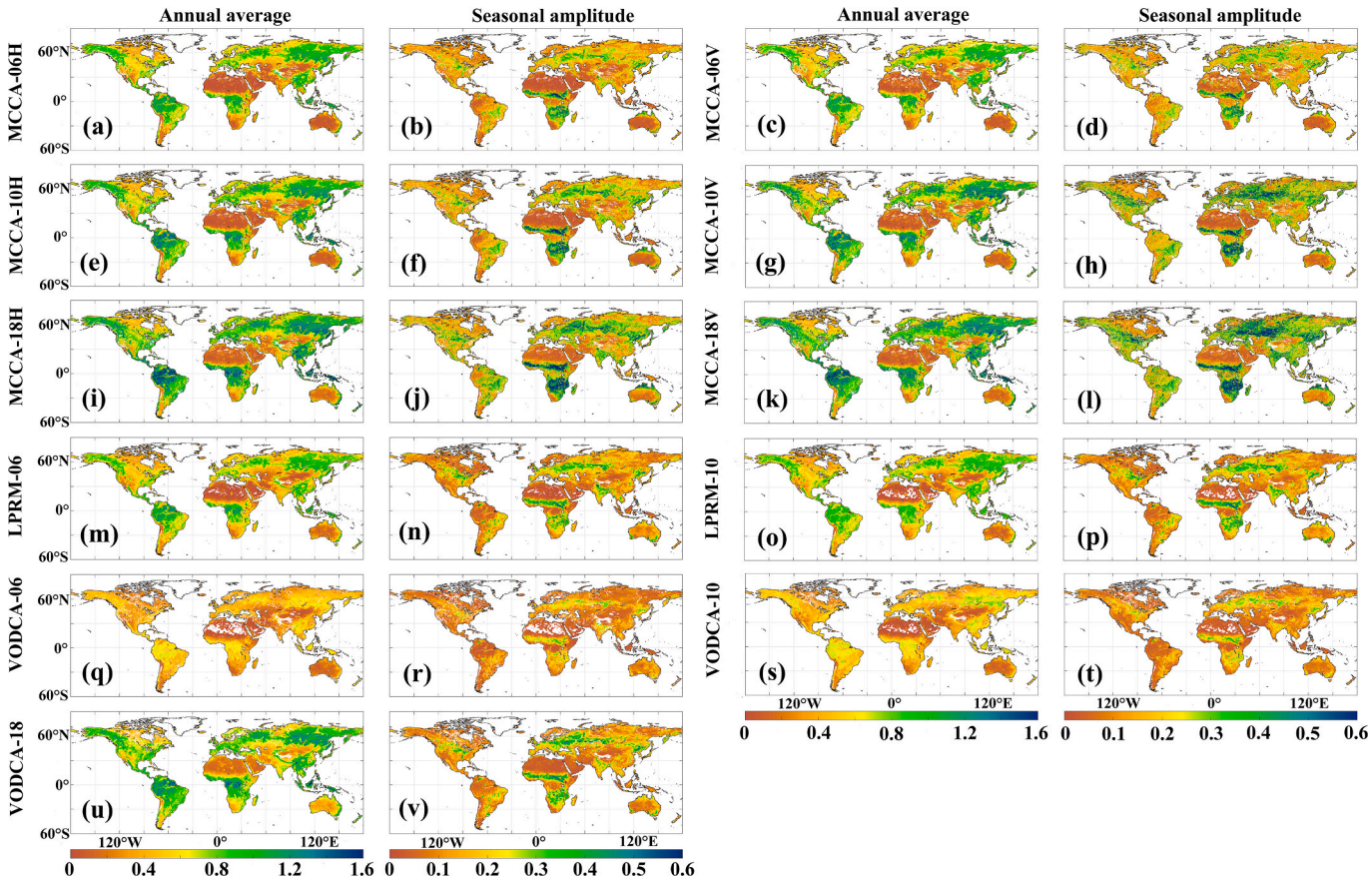

Fig. 3. Annual means and seasonal amplitudes of vegetation optical depth (VOD) averaged over the period from 2014 to 2016. (a-b) MCCA VOD-06H. (c-d) MCCA VOD-06V. (e-f) MCCA VOD-10H. (g-h) MCCA VOD-10V. (i-j) MCCA VOD-18H. (k-l) MCCA VOD-18V. (m-n) LPRM VOD-06. (o-p) LPRM VOD-10. (q-r) VODCA VOD-06. (s-t) VODCA VOD-10. (u-v) VODCA VOD-18. The marks ''06'', ''10'', and ''18'' denote the frequency of C-, X-, and Ku-bands, respectively. 'H' denotes the horizontal polarization, and 'V' denotes the vertical polarization.

the whole (Fig. 4). In contrast, forest areas show higher VOD values, especially the evergreen broadleaf forest which presents the highest VOD values. Notably, the MCCA VOD values increase with frequency for each land cover type, which is consistent with the physical expectation.

To better investigate the seasonal dynamics of different VOD products, we selected four pixels (Table 2) with different land cover types and climates to visualize the time series of data. The values of VOD were smoothed by applying a seven-day moving average, and each column

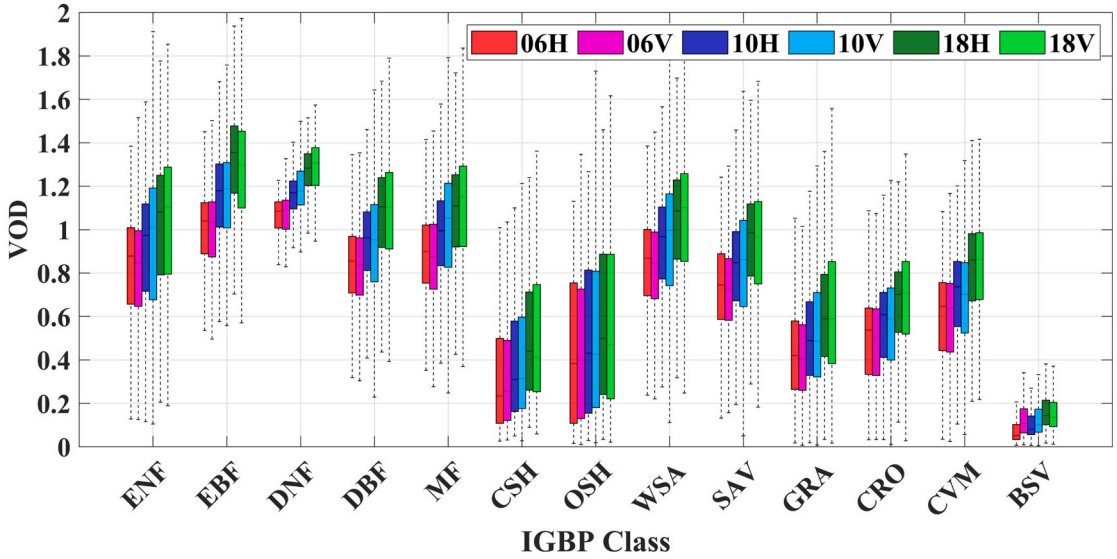

Fig. 4. Boxplot of time-averaged MCCA VODs for different IGBP classes and channels. The central mark within each box shows the median value, and the bottom and top edges mark the extent of the 25th and 75th percentiles. Whiskers include 99.3% of all data. The marks ''06'', ''10'', and ''18'' denote the frequency of C-, X-, and Ku-bands, respectively. 'H' denotes the horizontal polarization, and 'V' denotes the vertical polarization.

Table 2
Information on the selected four sites for vegetation optical depth (VOD) comparison.

Location	Latitude	Longitude	Climate zone	Dominate IGBP Class
USA	41.625° N	100.125° W	Cold, without dry season, hot Summer	Grassland
Congo	7.791° N	25.581° E	Tropical, savannah	Woody Savanna
Australia	36.375° S	141.625° E	Arid, steppe, cold	Cropland
Amazon	5.125° S	76.125° W	Tropical rainforest	Evergreen Broadleaf Forest

represents the VOD at different bands. The seasonal dynamics of all VOD products are synchronized well with NDVI except the Amazon forest site. For example, both VOD and NDVI peak in July or August and reach a minimum in January or February in the grassland of the USA and the cropland of Australia (Fig. 5 (a, c)). At the woody savanna site of Congo (Fig. 5(b)), after suffering a long period of drought, all the VOD data present a sharp upward trend at the beginning of the rainy days. This indicates that VOD can capture well the water variation in vegetation. Interestingly, there exists a small peak shape of MCCA-derived VODs at all channels from January to April 2015 at this site, which is highly consistent with NDVI. This phenomenon also occurs in the VOD products from LPRM at C-band and VODCA at Ku-band, but to a lesser extent than MCCA. In the Amazon forest site (Fig. 5 (d)), NDVI shows marginal seasonality throughout the year while MCCA and other VOD products show slight decreases from May to June. MCCA VODs are mostly higher than other VOD products at the four sites, while VODCA presents the lowest VOD values. To be noted, it is still challenging to validate the absolute value or accuracy of VOD, because it is a physical variable associated with the RTE and parameters used during the retrieval. Fig. 5 also shows that the seasonal fluctuation of VOD from MCCA in V polarization is larger than that in H polarization. The differences in MCCA VODs related to polarization and frequency are discussed in section 4.2.

3.2.2. *Spatial/temporal correlation between VOD and AGB/NDVI*

Fig. 6. illustrates the density plots of different VOD products compared with AGB circa 2015 developed by Saatchi et al. (2011) at the global scale. It is shown that VODs have different ranges due to the differences in their retrieval algorithms. There is a clear evolution in the scatter plots for different frequencies in MCCA VODs. In contrast, the scatter plots of C- and X-bands from VODCA and LPRM are almost identical for both frequencies, while Ku-VOD from VODCA is shifted to higher values. All the density scatter plots present similar patterns of VOD changing with AGB. VOD show a sign of saturation when the AGB

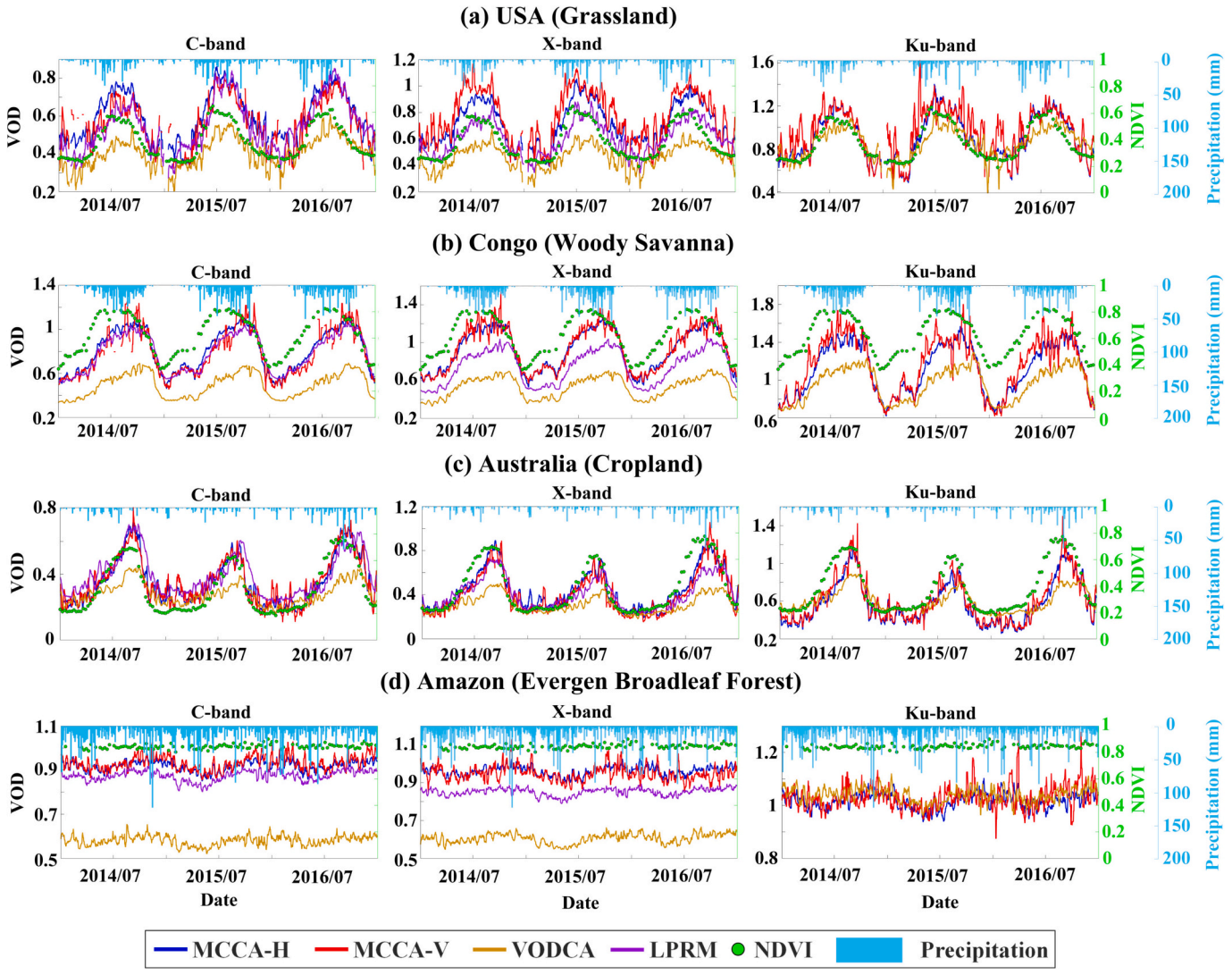

Fig. 5. Time series of different vegetation optical depth (VOD) (smoothed with a moving window filter of seven days) at C-, X- and Ku-bands at selected sites. (a) USA (b) Congo (c) Australia (d) Amazon.

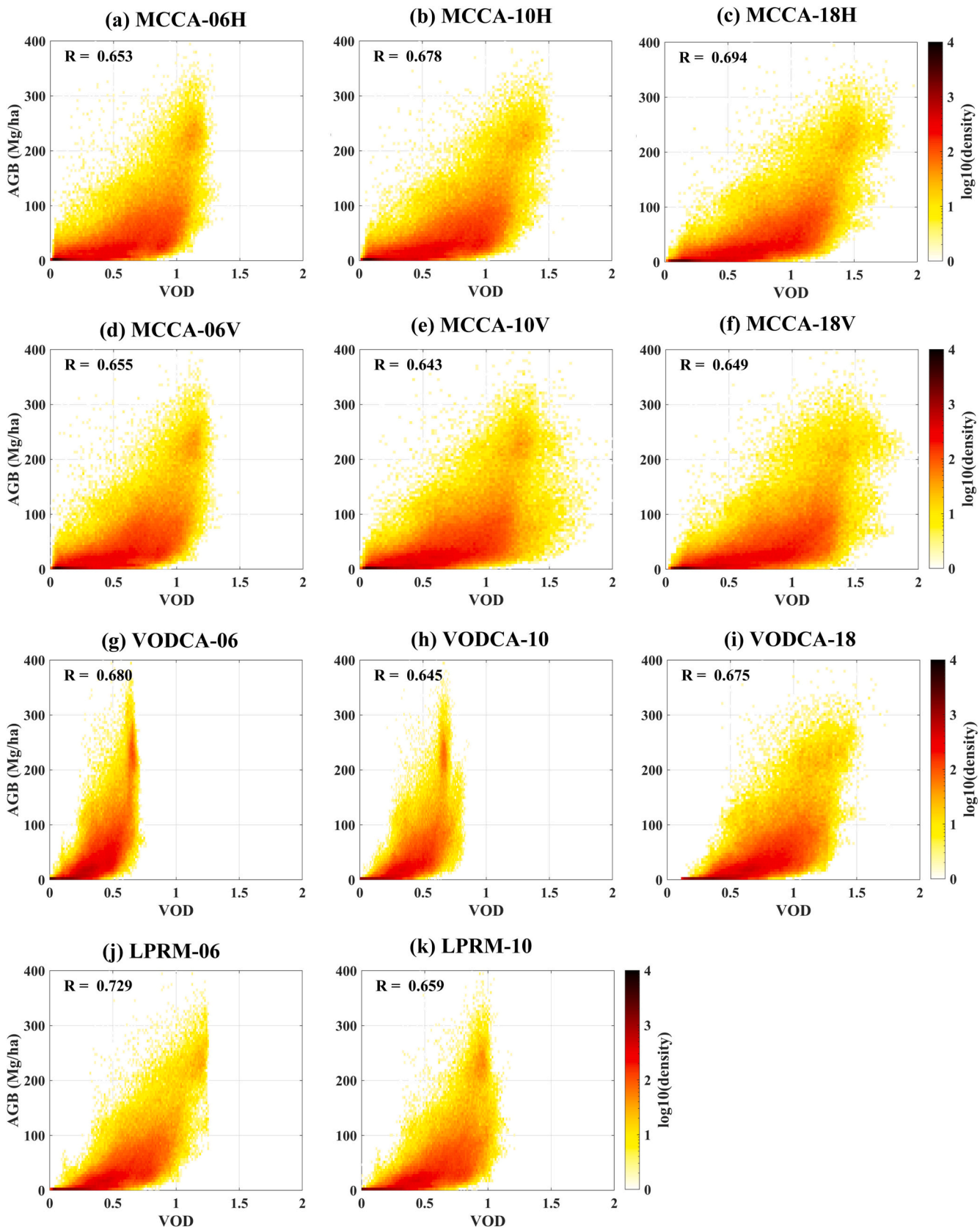

Fig. 6. Density scatter plots between vegetation optical depth (VOD) at different channels against Saatchi AGB at the global scale. R is the spatial correlation coefficient between VOD and AGB. The color bars are in the log10 scale. The marks ''06'', ''10'', and ''18'' denote the frequency of C-, X-, and Ku-bands, respectively. 'H' denotes the horizontal polarization, and 'V' denotes the vertical polarization.

exceeds 100 Mg/ha. At C- and X-bands, VODs from VODCA have a steep increase near AGB ~50 Mg/ha, while the other products show a gradual smooth slope transition. This is consistent with the finding reported by Li et al. (2021). H-polarized VODs from MCCA have higher values of spatial correlation with AGB than the V-polarized except for the C-band. At the C-band, LPRM VOD has the largest R value (0.729) with AGB, followed by VODCA (0.680), and V- and H-polarized VOD from MCCA (R = 0.655 and 0.653). At the X-band, H-polarized VOD from MCCA shows the highest R value (0.678) with AGB, followed by LPRM (R = 0.659), VODCA (R = 0.645), and V-polarized VOD from MCCA (R = 0.643). At the Ku-band, H-polarized VOD from MCCA shows the strongest correlation with AGB (R = 0.694), followed by VODCA (R = 0.675), and V-polarized VOD from MCCA (R = 0.649). The phenomenon that the sensitivity of VOD to biomass decreases with increasing frequency is not common or regular here among the C-, X- and Ku-band VODs. Since observations from these three bands are more dominated by the vegetation canopy, the discrepancy in the sensitivity of VOD to biomass may be more obvious among the L-, C-, and X-bands.

We also analyzed the spatial correlations of VODs with the long-term carbon density data developed by Xu et al. (2021) and made an intercomparison with the recently developed AMSR2-IB VOD product (Wang et al., 2021) at a regional scale (AMSR2-IB VOD is currently only available in Africa). As shown in Fig. B8-B10 in Appendix B, the difference in the correlation between VOD and AGB or carbon density is not significant. Theoretically, VOD is determined by both vegetation water potential and biomass. The relationship between VOD and AGB should be much more complex rather than the simple linear correlation. Since studies on how to physically infer AGB from VOD are still limited, it is expected MCCA derived polarization, and frequency-dependent VODs can provide a basis for further exploration.

Temporal correlations of VODs with NDVI were calculated for each pixel over the globe using synchronous 8-day data. As shown in Fig. B11 in Appendix B, different VOD products exhibit generally similar spatial patterns of temporal correlation (R) values with NDVI. All VOD products exhibit high R values in the Sahel region, Miombo woodlands, southeastern Brazil, and most of Europe and Russia. All VODs have non-significant correlations (p > 0.05) with NDVI over desert areas (e.g., the Sahara of Africa, desert areas in central Asia, and the Taklamakan in the northwest of China) and most of the tropical areas (e.g., Amazon and the Malay Archipelago). There are also some differences between MCCA and other VOD products in the temporal correlations with NDVI. MCCA VODs show relatively high significant correlations with NDVI in the equatorial region of Congo, while the other products are not significantly with NDVI. In addition, MCCA and other VOD products show the opposite correlations with NDVI in parts of southeast China, South Africa, and central and western Australia, and this is more obvious in the MCCA V-polarized VOD product. Special care should be taken when using VOD products to study vegetation phenology in these areas.

To further investigate the difference in the temporal correlations between VOD and NDVI, a map showing which VOD product has the strongest per-pixel correlation (absolute value) with NDVI for each frequency is presented in Fig. 7. At the C-band, MCCA VOD at H-polarization accounts for the largest proportion (30.17%) of pixels in which the correlation between VOD and NDVI are significant, followed by LPRM (27.09%), VODCA (21.50%) and MCCA-V (13.83%). At the X-band, MCCA VOD at H-polarization also exhibits the largest percentage (29.24%), followed by VODCA (24.98%), LPRM (22.11%) and MCCA-V (16.17%). At the Ku-band, the proportion of significant pixels in MCCA-H (38.09%) is slightly larger than that in VODCA (37.70%), while the proportion of MCCA-V (14.81%) is the smallest. The common areas, in which MCCA VODs at three frequencies have the stronger correlations with NDVI than other VOD products, are mainly concentrated in the south of the Sahel near the equator, Miombo woodlands, southeastern Brazil, Mexico, northeast China, and Indo-China Peninsula.

To explore the change of temporal correlation between VOD and NDVI with vegetation types, we aggregated the R values of each pixel based on the IGBP types (as shown in Fig. B12 in Appendix B). In general, all the V-polarized VODs from MCCA show slightly lower or comparable values of R than the H-polarized for all land cover types. As to the EBF type, VOD at all channels from MCCA show larger median R-values than VODCA and LPRM, but in CSH and OSH types, MCCA is much smaller than them. In the BSV type, MCCA also produces lower R values at C- and X-bands than VODCA and LPRM. But at Ku-band, both MCCA and VODCA have a wide range of R. More specifically, MCCA-H

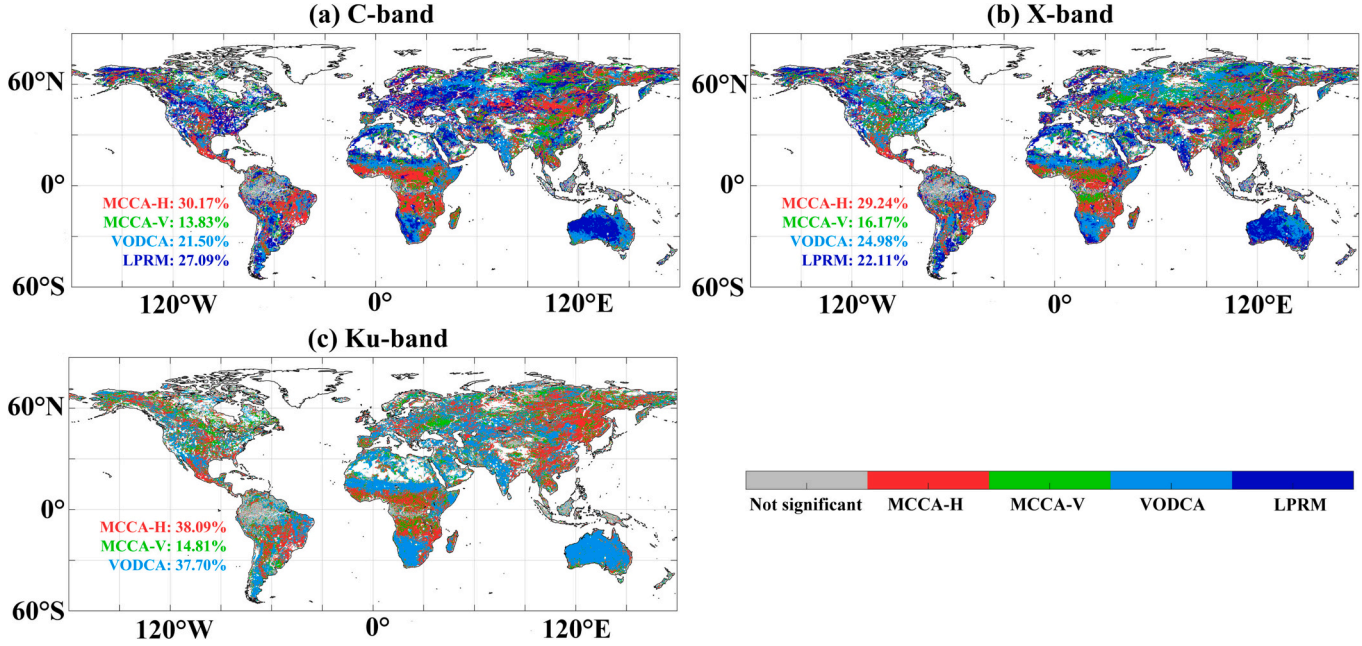

Fig. 7. Spatial distribution showing which vegetation optical depth (VOD) product produced the highest absolute temporal correlation (R) with MODIS NDVI over the period from 2014 to 2016 for (a) C-band; (b) X-band; (c) Ku-band. Grey areas correspond to the pixels where the temporal correlation between VOD and NDVI is not significant (p > 0.05). White areas denote "no valid data". Numbers on graphs indicate the percentage of pixels with the maximum R-value among all the significant pixels of each product.

VOD at C-band exhibits higher values of R than VODCA and LPRM in the WSA, SAV, GRA, and CVM types. For forest and cropland types (ENF, DNF, DBF, MF, CRO), both H and V-polarized VODs from MCCA show comparable or slightly lower R-values relative to VODCA and LPRM VOD. At the X-band, the correlation of MCCA VOD with NDVI is very similar to the C-band for different types. At the Ku-band, both H- and V-polarized VODs from MCCA show a higher median value of R than VODCA in the DNF type.

4. Discussion

4.1. Consistency analysis of SM

In this study, MCCA was implemented on the AMSR-E and AMSR2 observations to provide a long-term SM product at the global scale. Due to the different performance between AMSR-E and AMSR2, the inter-calibration over each grid cell was performed before retrieval to reduce the systematic error. However, cross-calibration cannot completely eliminate the potential differences in TB characteristics, and algorithm performance may vary between sensors. Thus, MCCA SM consistency was examined through statistical comparison of best-quality retrievals between the AMSR-E and AMSR2 parts of the dataset. For the descending retrievals, the global mean and standard deviation of SM from AMSR-E over the period 2002–2011 are 0.194 m^3/m^3 and 0.120 m^3/m^3, respectively, while those from AMSR2 over the period 2012–2021 are 0.195 m^3/m^3 and 0.121 m^3/m^3, respectively. For the ascending orbit, the corresponding values from AMSR-E are 0.186 m^3/m^3 and 0.120 m^3/m^3, respectively, while those from ASMR2 are 0.192 m^3/m^3 and 0.118 m^3/m^3, respectively. It is indicated that MCCA retrieved SM from AMSR-E and AMSR2 are consistent, especially in descending orbit.

To further evaluate the consistency of retrieved SM, the CDF of all the daily data from AMSR-E and AMSR2 are presented in Fig. 8. For the descending retrieval, both CDF curves are close to each other. For the ascending retrieval, the CDF of AMSR-E is slightly higher than that of AMSR2 when SM is in the range of 0.05–0.17 m^3/m^3. As a comparison, the CDF plots of other five SM products are shown in Fig. B13 in Appendix B. The CDF of AMSR-E is slightly higher than that of AMSR2 between 0.3 m^3/m^3 and 0.8 m^3/m^3 in the LPRM-C descending retrieval, while the CDF of AMSR-E is larger than that of AMSR2 overall in the ascending retrieval. For the LPRM-X descending retrieval, the CDF of AMSR-E is similar to that of AMSR2. For the LPRM-X ascending retrieval, the CDF of ASMR-E is slightly higher than that of AMSR2 in the range of 0–0.2 m^3/m^3. The SM product from JAXA shows good consistency between the two sensors for both descending and ascending orbits. The ANN product is only available for descending orbit, and the CDF from AMSR-E exhibits slightly higher levels than that of AMSR2. CCI-P SM is a merged product in that SM from different missions was rescaled through the CDF matching, so it exhibits a high degree of consistency between the two periods (2002–2011 and 2012–2021). Overall, these evidences suggest that MCCA-derived SM from AMSR-E and AMSR2 has a good consistency.

4.2. Dependence of VOD on polarization and frequency

The crucial feature of MCCA is that it adopts a self-constraint strategy and combines the multi-channel information to retrieve SM first and then uses the retrieved SM as input to estimate the multi-channel VODs by reversing the RTE. In the previous section 3.2.1, we presented the spatial and temporal patterns of MCCA-derived multi-channel VODs. To further explore the dependence of MCCA VODs on polarization and frequency, annual averages of polarization difference and frequency gradient based on per-pixel were calculated from the MCCA descending retrievals over three years (2014–2016). The polarization difference refers to the value of vertical polarized VOD minus the horizontal polarized one, and frequency difference refers to the value of high-frequency VOD minus the low-frequency one.

Fig. 9. shows the annual averages and seasonal amplitudes of polarization differences among MCCA VODs. In North America along the Rocky Mountain region, Alaska, Kazakhstan, and most of Russia and the Indian peninsula, the polarization differences are negative at C-band while positive at X- and Ku-bands. In contrast, in northeastern Canada and the northern Russian region near the Kara Sea, the polarization differences at C-band present positive values while negative at X- and Ku-bands. In addition, in northern Africa and most of Australia, the polarization difference appears positive for C- and X-bands, but negative or close to zero for the Ku-band.

The seasonal amplitudes of polarization difference show similar patterns across the three bands over most regions of the globe. At the Ku-band, the seasonal amplitude of polarization difference exhibits the highest values over the central and eastern United States, western Russia, and Europe. It seems that seasonal fluctuation in polarization difference is more susceptible to vegetation, and the higher the frequency, the greater the fluctuation. It should be pointed out that RFI was examined here with spectral indices ($TB_{Low\ Frequency} - TB_{High\ Frequency} > 5\ K$) as previous studies (Li et al., 2004; Njoku et al., 2005). However, the spectral gradient difference within 5 K may be associated with the weak RFI that is difficult to detect, or it may be

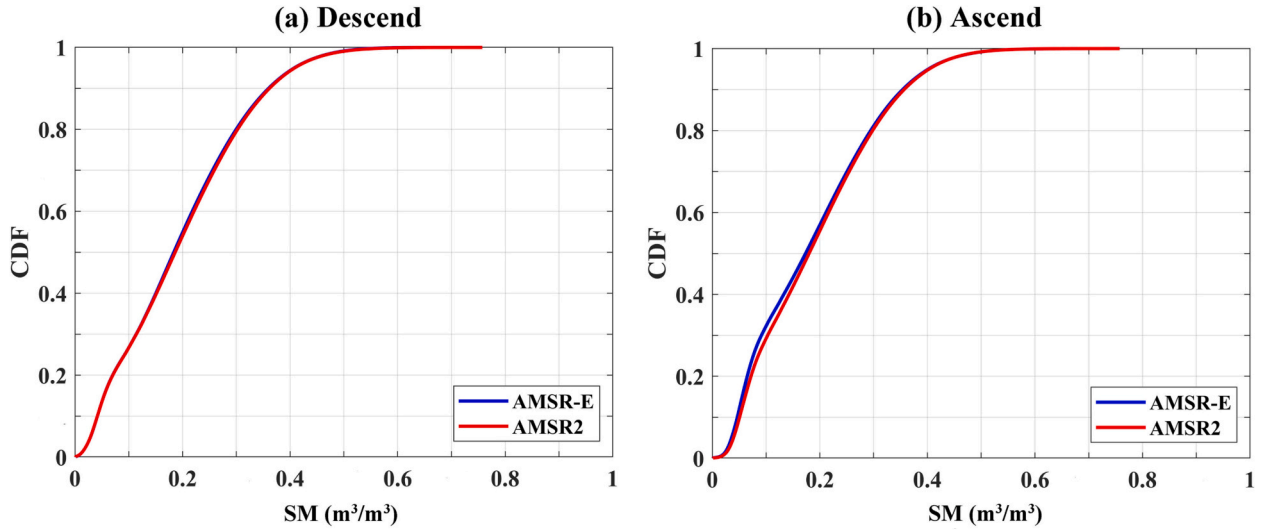

Fig. 8. Cumulative distribution functions (CDF) of MCCA retrieved soil moisture from AMSR-E and AMSR2 for (a) Descending orbit; (b) Ascending orbit.

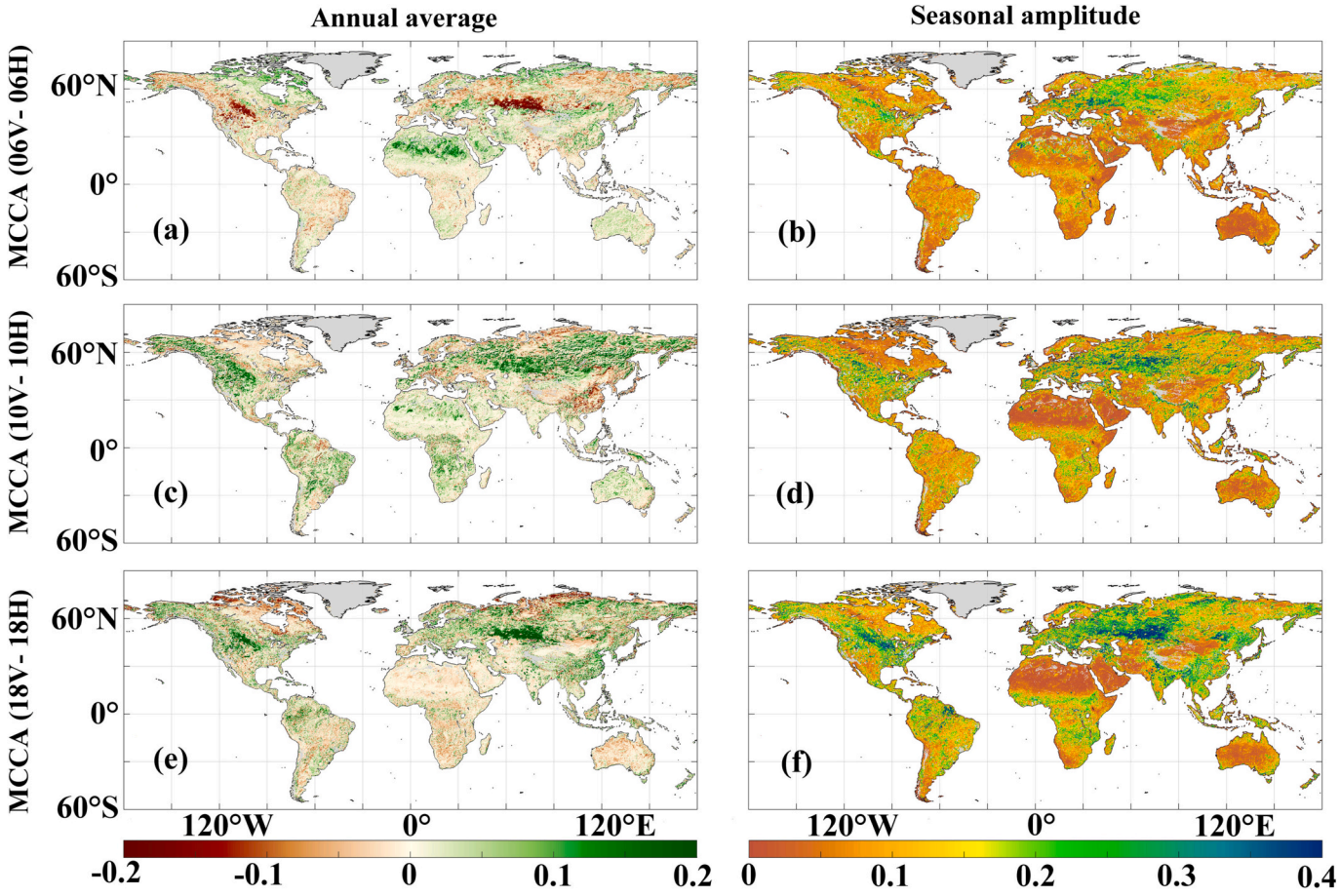

Fig. 9. Annual means and seasonal amplitudes of polarization difference between V- and H-polarized vegetation optical depth (VOD) averaged over the period from 2014 to 2016. (a-b) MCCA VOD-06V minus VOD-06H; (c-d) MCCA VOD-10V minus VOD-10H; (e-f) MCCA VOD-18V minus VOD-18H. Grey areas correspond to the land pixels with "no valid data". The marks ''06'', ''10'', and ''18'' denote the frequency of C-, X-, and Ku-bands, respectively. 'H' denotes the horizontal polarization, and 'V' denotes the vertical polarization.

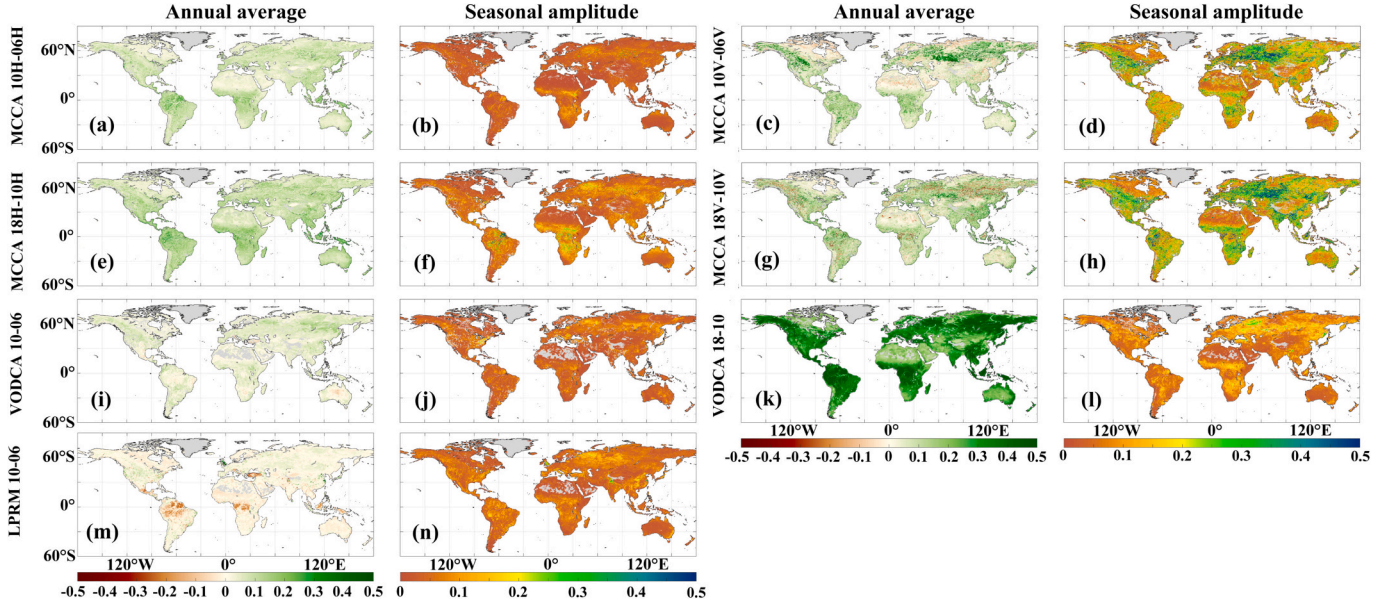

Fig. 10. Annual means and seasonal amplitudes of frequency difference among VODs averaged over the period from 2014 to 2016. (a-b) MCCA VOD-10H minus VOD-06H; (c-d) MCCA VOD-10V minus VOD-06V; (e-f) MCCA VOD-18H minus VOD-10H; (g-h) MCCA VOD-18V minus VOD-10V; (i-j) VODCA VOD-10 minus VOD-06; (k-l) VODCA VOD-18 minus VOD-10; (m-n) LPRM VOD-10 minus VOD-06. Grey areas correspond to the land pixels with "no valid data". The marks ''06'', ''10'', and ''18'' denote the frequency of C-, X-, and Ku-bands, respectively. 'H' denotes the horizontal polarization, and 'V' denotes the vertical polarization.

associated with a physical characteristic of strong scattering effects. It is argued by Njoku et al. (2005) that volume and surface scattering can cause surface emissivity to decrease with increasing frequency in some cases. Therefore, the polarization difference of VOD at C-, X- and Ku-bands identified in this study can be attributed to either the realistic vegetation physics or imperfection of the zero-order RTE used in MCCA.

Fig. 10. presents the annual averages and seasonal amplitudes of frequency difference among different VOD products. It is found that MCCA VOD at high frequency is generally larger than the low frequency in the horizontal polarization. However, MCCA VOD at high frequency shows smaller values than that at low frequency over some regions for the vertical polarization. For the VODCA products, X-VOD shows slightly lower values than C-VOD in Mexico, Turkey, Italy, east-central Australia, parts of South Africa, and Brazil. But for the comparison between X- and Ku-bands from VODCA, Ku-VOD is significantly larger than X-VOD. The frequency difference between C-VOD and X-VOD in the LPRM product is not distinct in most of the globe, except in the Amazon, Congo, Southeast Asia, Mexico, Italy, and Turkey, in which X-VOD shows lower values than C-VOD. It is acknowledged that values of VOD increase with frequency. For the VODCA products, the pre-merged VODs were first retrieved from the same algorithm as the NASA LPRM product but with a different version (LPRM V6) and then merged by the CDF matching (Moesinger et al., 2020). The rescaling method used in VODCA can distinguish the differences between different frequencies but requires a reference data source (AMSR-E is the reference in VODCA). Similarly, the VOD relationship between different channels (Eq. (5)) used in MCCA can also ensure that the value of VOD at high frequency is greater than that at low frequency. More importantly, it is an inherent feature of MCCA, which makes the magnitude discrepancy between multi-frequency VOD more reasonable.

Regarding the seasonal variation, the difference between MCCA VOD-10H and MCCA VOD-06H presents small seasonal amplitudes, similar to those of VODCA and LPRM. The seasonal amplitude of the difference between MCCA VOD-18H and MCCA VOD-10H is slightly larger than the seasonal amplitude of the difference between MCCA VOD-10H and MCCA VOD-06H in parts of Amazon, Sahel, Congo, Miombo woodlands, and western Russia, and is similar to that of the difference between VODCA VOD-18 and VODCA VOD-10. In contrast, the frequency difference from MCCA VOD in vertical polarization exhibits large seasonal variation.

5. Conclusion

This paper presented a new SM and frequency- and polarization-dependent VOD product using the MCCA algorithm based on the inter-calibrated AMSR-E/2 observations. The main feature of MCCA in this study is that it can fully utilize the multi-frequency and dual-polarization information for retrieving SM and then estimate frequency- and polarization-dependent VODs through reversing RTE. The retrieved SM from MCCA was inter-compared with the ANN, CCI-P, LPRM-C, LPRM-X and JAXA SM products over 25 dense SM networks. While quantitative assessment of VOD is still challenging, MCCA-derived VODs and other two VOD products (LPRM and VODCA), were indirectly evaluated against the vegetation AGB and MODIS NDVI.

Overall, MCCA showed good performance on both SM and VOD. According to the validation results over 25 dense SM networks, MCCA-derived SM produced the lowest values of ubRMSE over most of networks (9/25), same as ANN SM. In the overall comparison of 25 networks, MCCA achieved the best scores in terms of RMSE (0.074 m^3/m^3), ubRMSE (0.073 m^3/m^3) and bias (0.007 m^3/m^3), and presented slightly lower value of R (0.709) than LPRM-X ($R = 0.735$). With respected to the inter-comparison among different VOD products, MCCA-derived VODs were comparable to the LPRM and VODCA VOD products in terms of the spatial correlation with AGB and the temporal correlation with NDVI. In addition, H-polarized VODs from MCCA showed more sensitive to vegetation than the V-polarized ones. More importantly, MCCA presented very reasonable variations across the microwave spectrum, while LPRM products cannot show the increase of VOD with frequency as theoretical expectation. Although the frequency difference was also distinct among the VODCA products, it was a manipulated phenomenon due to the CDF matching technology used in VODCA.

It is expected that the new SM and VOD product may provide new insights for better understanding water fluxes in the soil-plant-atmosphere continuum. In addition, the retrieval was implemented on snapshot observations, thus MCCA can provide continuous daily data once the daily TB is updated. Furthermore, MCCA can be extended to other similar multi-frequency sensors, such as FY-3B/C/D/F/G or the scheduled AMSR3 and CIMR in the future.

Authorship contribution statement

- **Lu Hu**: Software, Writing – original draft, Formal analysis, Data curation, Investigation, Validation
- **Tianjie Zhao**: Conceptualization, Investigation, Writing – review & editing
- **Weimin Ju**: Writing – review & editing, Supervision, Funding acquisition, Resources
- **Zhiqing Peng**: Software, Formal analysis, Data curation
- **Jiancheng Shi**: Formal analysis, Writing – review & editing, Funding acquisition
- **Nemesio J. Rodríguez-Fernández**: Formal analysis, Writing – review & editing
- **Jean-Pierre Wigneron**: Formal analysis, Writing – review & editing
- **Michael H. Cosh**: Data Curation, Writing – review & editing
- **Kun Yang**: Writing – review & editing
- **Hui Lu**: Writing – review & editing
- **Panpan Yao**: Data curation

Declaration of Competing Interest

The authors declare that they have no known competing financial interests or personal relationships that could have appeared to influence the work reported in this paper.

Data availability

The AMSR-E/2 soil moisture and vegetation optical depth product using MCCA were jointly developed by the International Institute for Earth System Science, Nanjing University, and the Aerospace information research institute, Chinese Academy of Sciences. The dataset is available at the National Tibetan Plateau/Third Pole Environment Data Center (https://doi.org/10.11888/Terre.tpdc.272907).

Acknowledgments

This study was jointly supported by the National Key Research and Development Program of China (No. 2021YFB3900104), National Natural Science Foundation of China (No. 42141005), and in part by the Second Tibetan Plateau Scientific Expedition and Research Program (No. 2019QZKK0206). USDA is an equal opportunity provider and employer. This research was a contribution in part from the Long-Term Agroecosystem Research (LTAR) network. LTAR is supported by the United States Department of Agriculture. The authors sincerely thank Prof. Sassan S. Saatchi for providing the AGB data.

Appendix A. Supplementary data

Supplementary data to this article can be found online at https://doi.org/10.1016/j.rse.2023.113595.

References

Al Bitar, A., Mialon, A., Kerr, Y.H., Cabot, F., Richaume, P., Jacquette, E., Quesney, A., Mahmoodi, A., Tarot, S., Parrens, M., Al-Yaari, A., Pellarin, T., Rodriguez-Fernandez, N., Wigneron, J.-P., 2017. The global SMOS level 3 daily soil moisture and brightness temperature maps. Earth Syst.Sci. Data 9, 293–315.

Chen, Y., Yang, K., Qin, J., Zhao, L., Tang, W., Han, M., 2013. Evaluation of AMSR-E retrievals and GLDAS simulations against observations of a soil moisture network on the central Tibetan plateau. J. Geophys. Res. Atmos. 118, 4466–4475.

Chen, Y.Y., Yang, K., Qin, J., Cui, Q., Lu, H., La, Z., Han, M.L., Tang, W.J., 2017. Evaluation of SMAP, SMOS, and AMSR2 soil moisture retrievals against observations from two networks on the Tibetan plateau. J. Geophys. Res.-Atmos. 122, 5780–5792.

Colliander, A., Jackson, T.J., Bindlish, R., Chan, S., Das, N., Kim, S.B., Cosh, M.H., Dunbar, R.S., Dang, L., Pashaian, L., Asanuma, J., Aida, K., Berg, A., Rowlandson, T., Bosch, D., Caldwell, T., Caylor, K., Goodrich, D., Jassar, H., Lopez-Baeza, E., Martinez-Fernandez, J., Gonzalez-Zamora, A., Livingston, S., McNairn, H., Pacheco, A., Moghaddam, M., Montzka, C., Notarnicola, C., Niedrist, G., Pellarin, T., Prueger, J., Pulliainen, J., Rautiainen, K., Ramos, J., Seyfried, M., Starks, P., Su, Z., Zeng, Y., van der Velde, R., Thibeault, M., Dorigo, W., Vreugdenhil, M., Walker, J.P., Wu, X., Monerris, A., O'Neill, P.E., Entekhabi, D., Njoku, E.G., Yueh, S., 2017. Validation of SMAP surface soil moisture products with core validation sites. Remote Sens. Environ. 191, 215–231.

Cui, H., Jiang, L., Du, J., Zhao, S., Wang, G., Lu, Z., Wang, J., 2017. Evaluation and analysis of AMSR-2, SMOS, and SMAP soil moisture products in the Genhe area of China. J. Geophys. Res. Atmos. 122, 8650–8666.

Didan, K., 2015. MOD13C1 MODIS/Terra Vegetation Indices 16-Day L3 Global 0.05Deg CMG V006. NASA EOSDIS Land Processes DAAC.

Didan, K., 2015. MYD13C1 MODIS/Aqua Vegetation Indices 16-Day L3 Global 0.05Deg CMG V006. NASA EOSDIS Land Processes DAAC.

Dorigo, W., Wagner, W., Albergel, C., Albrecht, F., Balsamo, G., Brocca, L., Chung, D., Ertl, M., Forkel, M., Gruber, A., Haas, E., Hamer, P.D., Hirschi, M., Ikonen, J., de Jeu, R., Kidd, R., Lahoz, W., Liu, Y.Y., Miralles, D., Mistelbauer, T., Nicolai-Shaw, N., Parinussa, R., Pratola, C., Reimer, C., van der Schalie, R., Seneviratne, S.I., Smolander, T., Lecomte, P., 2017. ESA CCI soil moisture for improved earth system understanding: state-of-the art and future directions. Remote Sens. Environ. 203, 185–215.

Dorigo, W.A., Wagner, W., Hohensinn, R., Hahn, S., Paulik, C., Xaver, A., Gruber, A., Drusch, M., Mecklenburg, S., van Oevelen, P., Robock, A., Jackson, T., 2011. The international soil moisture network: a data hosting facility for global in situ soil moisture measurements. Hydrol. Earth Syst. Sci. 15, 1675–1698.

Drusch, M., 2007. Initializing numerical weather prediction models with satellite-derived surface soil moisture: data assimilation experiments with ECMWF's integrated forecast system and the TMI soil moisture data set. J. Geophys. Res. Atmos. 112.

Entekhabi, D., Njoku, E.G., Neill, P.E.O., Kellogg, K.H., Crow, W.T., Edelstein, W.N., Entin, J.K., Goodman, S.D., Jackson, T.J., Johnson, J., Kimball, J., Piepmeier, J.R., Koster, R.D., Martin, N., McDonald, K.C., Moghaddam, M., Moran, S., Reichle, R., Shi, J.C., Spencer, M.W., Thurman, S.W., Tsang, L., Zyl, J.V., 2010. The soil moisture active passive (SMAP) mission. Proc. IEEE 98, 704–716.

Fan, L., Wigneron, J.-P., Ciais, P., Chave, J., Brandt, M., Fensholt, R., Saatchi, S.S., Bastos, A., Al-Yaari, A., Hufkens, K., Qin, Y., Xiao, X., Chen, C., Myneni, R.B., Fernandez-Moran, R., Mialon, A., Rodriguez-Fernandez, N.J., Kerr, Y., Tian, F., Peñuelas, J., 2019. Satellite-observed pantropical carbon dynamics. Nat. Plants 5, 944–951.

Fan, L., Wigneron, J.-P., Ciais, P., Chave, J., Brandt, M., Sitch, S., Yue, C., Bastos, A., Li, X., Qin, Y., Yuan, W., Schepaschenko, D., Mukhortova, L., Li, X., Liu, X., Wang, M., Frappart, F., Xiao, X., Chen, J., Ma, M., Wen, J., Chen, X., Yang, H., van Wees, D., Fensholt, R., 2023. Siberian carbon sink reduced by forest disturbances. Nat. Geosci. 16, 56–62.

Feldman, A.F., Akbar, R., Entekhabi, D., 2018. Characterization of higher-order scattering from vegetation with SMAP measurements. Remote Sens. Environ. 219, 324–338.

Fernandez-Moran, R., Al-Yaari, A., Mialon, A., Mahmoodi, A., Al Bitar, A., De Lannoy, G., Rodriguez-Fernandez, N., Lopez-Baeza, E., Kerr, Y., Wigneron, J.-P., 2017. SMOS-IC: an alternative SMOS soil moisture and vegetation optical depth product. Remote Sens. 9, 457.

Friedl, M., Sulla-Menashe, D., 2019. MCD12Q1 MODIS/Terra+Aqua Land Cover Type Yearly L3 Global 500m SIN Grid V006. NASA EOSDIS Land Processes DAA.

Fujii, H., Koike, T., Imaoka, K., 2009. Improvement of the AMSR-E algorithm for soil moisture estimation by introducing a fractional vegetation coverage dataset derived from MODIS data. J. Remote Sens. Soc. Jpn. 29, 282–292.

Grant, J.P., Wigneron, J.P., De Jeu, R.A.M., Lawrence, H., Mialon, A., Richaume, P., Al Bitar, A., Drusch, M., van Marle, M.J.E., Kerr, Y., 2016. Comparison of SMOS and AMSR-E vegetation optical depth to four MODIS-based vegetation indices. Remote Sens. Environ. 172, 87–100.

Griend, A.A.V.D., Manfred Owe, J.D.R., Gouweleeuw, B., 1996. Measurement and behavior of dual-polarization vegetation optical depth and single scattering albedo at 1.4- and 5-GHz microwave frequencies. IEEE Trans. Geosci. Remote Sens. 34, 957–965.

Gruber, A., Scanlon, T., van der Schalie, R., Wagner, W., Dorigo, W., 2019. Evolution of the ESA CCI soil moisture climate data records and their underlying merging methodology. Earth Syst. Sci. Data 11, 717–739.

Holmes, T.R.H., De Jeu, R.A.M., Owe, M., Dolman, A.J., 2009. Land surface temperature from ka band (37 GHz) passive microwave observations. J. Geophys. Res.-Atmos. 114.

Houser, P.R., Shuttleworth, W.J., Famiglietti, J.S., Gupta, H.V., Syed, K.H., Goodrich, D. C., 1998. Integration of soil moisture remote sensing and hydrologic modeling using data assimilation. Water Resour. Res. 34, 3405–3420.

Huffman, G.J., Stocker, E.F., Bolvin, D.T., Nelkin, E.J., Tan, J., 2019. GPM IMERG Final Precipitation L3 1 day 0.1 degree x 0.1 degree V06. Goddard Earth Sciences Data and Information Services Center (GES DISC).

Imaoka, K., Maeda, T., Kachi, M., Kasahara, M., Ito, N., Nakagawa, K., 2012. Status of AMSR2 instrument on GCOM-W1. SPIE.

Jackson, T.J., 1993. Measuring surface soil-moisture using passive microwave remote-sensing. 3. Hydrol. Process. 7, 139–152.

Jackson, T.J., Cosh, M.H., Bindlish, R., Starks, P.J., Bosch, D.D., Seyfried, M., Goodrich, D.C., Moran, M.S., Du, J.Y., 2010. Validation of advanced microwave scanning radiometer soil moisture products. IEEE Trans. Geosci. Remote Sens. 48, 4256–4272.

Jackson, T.J., Hsu, A.Y., Van de Griend, A., Eagleman, J.R., 2004. Skylab L-band microwave radiometer observations of soil moisture revisited. Int. J. Remote Sens. 25, 2585–2606.

Jackson, T.J., Schmugge, T.J., 1991. Vegetation effects on the microwave emission of soils. Remote Sens. Environ. 36, 203–212.

Jones, M.O., Jones, L.A., Kimball, J.S., McDonald, K.C., 2011. Satellite passive microwave remote sensing for monitoring global land surface phenology. Remote Sens. Environ. 115, 1102–1114.

Karthikeyan, L., Pan, M., Konings, A.G., Piles, M., Fernandez-Moran, R., Nagesh Kumar, D., Wood, E.F., 2019. Simultaneous retrieval of global scale vegetation optical depth, surface roughness, and soil moisture using X-band AMSR-E observations. Remote Sens. Environ. 234, 111473.

Kawanishi, T., Sezai, T., Ito, Y., Imaoka, K., Takeshima, T., Ishido, Y., Shibata, A., Miura, M., Inahata, H., Spencer, R.W., 2003. The advanced microwave scanning radiometer for the earth observing system (AMSR-E), NASDA's contribution to the EOS for global energy and water cycle studies. IEEE Trans. Geosci. Remote Sens. 41, 184–194.

Kerr, Y.H., Waldteufel, P., Wigneron, J.P., Delwart, S., Cabot, F., Boutin, J., Escorihuela, M.J., Font, J., Reul, N., Gruhier, C., Juglea, S.E., Drinkwater, M.R., Hahne, A., Martín-Neira, M., Mecklenburg, S., 2010. The SMOS Mission: new tool for monitoring key elements ofthe global water cycle. Proc. IEEE 98, 666–687.

Koike, T., Nakamura, Y., Kaihotsu, I., Davaa, G., Matsuura, N., Tamagawa, K., Fujii, H., 2004. Development of an advanced microwave scanning radiometer (AMSR-E) algorithm of soil moisture and vegetation water content. Proc. Hydraul. Eng. 48, 217–222.

Konings, A.G., Piles, M., Das, N., Entekhabi, D., 2017. L-band vegetation optical depth and effective scattering albedo estimation from SMAP. Remote Sens. Environ. 198, 460–470.

Konings, A.G., Rao, K., Steele-Dunne, S.C., 2019. Macro to micro: microwave remote sensing of plant water content for physiology and ecology. New Phytol. 223, 1166–1172.

Konings, A.G., Saatchi, S.S., Frankenberg, C., Keller, M., Leshyk, V., Anderegg, W.R.L., Humphrey, V., Matheny, A.M., Trugman, A., Sack, L., Agee, E., Barnes, M.L., Binks, O., Cawse-Nicholson, K., Christoffersen, B.O., Entekhabi, D., Gentine, P., Holtzman, N.M., Katul, G.G., Liu, Y., Longo, M., Martinez-Vilalta, J., McDowell, N., Meir, P., Mencuccini, M., Mrad, A., Novick, K.A., Oliveira, R.S., Siqueira, P., Steele-Dunne, S.C., Thompson, D.R., Wang, Y., Wehr, R., Wood, J.D., Xu, X., Zuidema, P.A., 2021. Detecting forest response to droughts with global observations of vegetation water content. Glob. Chang. Biol. 27, 6005–6024.

Li, L., Njoku, E.G., Im, E., Chang, P.S., Germain, K.S., 2004. A preliminary survey of radio-frequency interference over the U.S. In aqua AMSR-E data. IEEE Trans. Geosci. Remote Sens. 42, 380–390.

Li, X., Wigneron, J.-P., Frappart, F., Fan, L., Ciais, P., Fensholt, R., Entekhabi, D., Brandt, M., Konings, A.G., Liu, X., Wang, M., Al-Yaari, A., Moisy, C., 2021. Global-scale assessment and inter-comparison of recently developed/reprocessed microwave satellite vegetation optical depth products. Remote Sens. Environ. 253, 112208.

Liu, Y.Y., van Dijk, A.I.J.M., de Jeu, R.A.M., Canadell, J.G., McCabe, M.F., Evans, J.P., Wang, G., 2015. Recent reversal in loss of global terrestrial biomass. Nat. Clim. Chang. 5, 470–474.

Ma, H., Zeng, J., Chen, N., Zhang, X., Cosh, M.H., Wang, W., 2019. Satellite surface soil moisture from SMAP, SMOS, AMSR2 and ESA CCI: a comprehensive assessment using global ground-based observations. Remote Sens. Environ. 231, 11121.

Meesters, A.G.C.A., DeJeu, R.A.M., Owe, M., 2005. Analytical derivation of the vegetation optical depth from the microwave polarization difference index. IEEE Geosci. Remote Sens. Lett. 2, 121–123.

Mironov, V.L., Dobson, M.C., Kaupp, V.H., Komarov, S.A., Kleshchenko, V.N., 2004. Generalized refractive mixing dielectric model for moist soils. IEEE Trans. Geosci. Remote Sens. 42, 773–785.

Mladenova, I.E., Jackson, T.J., Njoku, E., Bindlish, R., Chan, S., Cosh, M.H., Holmes, T.R. H., de Jeu, R.A.M., Jones, L., Kimball, J., Paloscia, S., Santi, E., 2014. Remote monitoring of soil moisture using passive microwave-based techniques — theoretical basis and overview of selected algorithms for AMSR-E. Remote Sens. Environ. 144, 197–213.

Mo, T., Choudhury, B.J., Schmugge, T.J., Wang, J.R., Jackson, T.J., 1982. A model for microwave emission from vegetation-covered fields. J. Geophys. Res. Oceans 87, 1229–1237.

Moesinger, L., Dorigo, W., de Jeu, R., van der Schalie, R., Scanlon, T., Teubner, I., Forkel, M., 2020. The global long-term microwave vegetation optical depth climate archive (VODCA). Earth Syst. Sci. Data 12, 177–196.

Mohanty, B.P., Cosh, M.H., Lakshmi, V., Montzka, C., 2017. Soil moisture remote sensing: state-of-the-science. Vadose Zone J. 16 vzj2016.2010.0105.

Njoku, E.G., Ashcroft, P., Chan, T.K., Li, L., 2005. Global survey and statistics of radio-frequency interference in AMSR-E land observations. IEEE Trans. Geosci. Remote Sens. 43, 938–947.
Njoku, E.G., Jackson, T.J., Lakshmi, V., Chan, T.K., Nghiem, S.V., 2003. Soil moisture retrieval from AMSR-E. IEEE Trans. Geosci. Remote Sens. 41, 215–229.
Njoku, E.G., Li, L., 1999. Retrieval of land surface parameters using passive microwave measurements at 6–18 GHz. IEEE Trans. Geosci. Remote Sens. 37, 79–93.
Owe, M., de Jeu, R., Holmes, T., 2008. Multisensor historical climatology of satellite-derived global land surface moisture. J. Geophys. Res. Earth Surf. 113.
Jeu, Richard, Owe, M., 2011. AMSR-E/Aqua surface soil moisture (LPRM) L3 1 day 25 km x 25 km descending V002. In: Goddard Earth Sciences Data and Information Services Center (GES DISC). Accessed: 10.5067/MXL0MFDHWP07.
Jeu, Richard, Owe, M., 2014. AMSR2/GCOM-W1 surface soil moisture (LPRM) L3 1 day 25 km x 25 km descending V001. Goddard Earth Sciences Data and Information Services Center (GES DISC). Accessed: 10.5067/CGDEOBASZ178.
Saatchi, S.S., Harris, N.L., Brown, S., Lefsky, M., Mitchard, E.T., Salas, W., Zutta, B.R., Buermann, W., Lewis, S.L., Hagen, S., Petrova, S., White, L., Silman, M., Morel, A., 2011. Benchmark map of forest carbon stocks in tropical regions across three continents. Proc. Natl. Acad. Sci. U. S. A. 108, 9899–9904.
Shi, J., Jackson, T., Tao, J., Du, J., Bindlish, R., Lu, L., Chen, K., 2008. Microwave vegetation indices for short vegetation covers from satellite passive microwave sensor AMSR-E. Remote Sens. Environ. 112, 4285–4300.
Shi, J., Jiang, L., Zhang, L., Chen, K.-S., Wigneron, J.P., Chanzy, A., 2005. A parameterized multifrequency-polarization surface emission model. IEEE Trans. Geosci. Remote Sens. 43, 2831–2841.
Ulaby, F.T., Wilson, E.A., 1985. Microwave attenuation properties of vegetation canopies. IEEE Trans. Geosci. Remote Sens. GE-23, 746–753.
Van de Griend, A.A., Wigneron, J.P., 2004. The b-factor as a function of frequency and canopy type at H-polarization. IEEE Trans. Geosci. Remote Sens. 42, 786–794.
Van der Schalie, R., Parinussa, R.M., Renzullo, L.J., van Dijk, A.I.J.M., Su, C.H., de Jeu, R.A.M., 2015. SMOS soil moisture retrievals using the land parameter retrieval model: evaluation over the Murrumbidgee catchment, Southeast Australia. Remote Sens. Environ. 163, 70–79.
Wanders, N., Bierkens, M.F.P., de Jong, S.M., de Roo, A., Karssenberg, D., 2014. The benefits of using remotely sensed soil moisture in parameter identification of large-scale hydrological models. Water Resour. Res. 50, 6874–6891.
Wang, M.J., Fan, L., Frappart, F., Ciais, P., Sun, R., Liu, Y., Li, X.J., Liu, X.Z., Moisy, C., Wigneron, J.P., 2021. An alternative AMSR2 vegetation optical depth for monitoring vegetation at large scales. Remote Sens. Environ. 263.
Wieder, W.R., Boehnert, J., Bonan, G.B., Langseth, M., 2014. Regridded Harmonized World Soil Database v1.2. Oak Ridge National Laboratory Distributed Active Archive Center, Oak Ridge, Tennessee, USA. Available on-line [http://daac.ornl.gov] from.
Wigneron, J.P., Chanzy, A., Calvet, J.C., Bruguier, W., 1995. A simple algorithm to retrieve soil-moisture and vegetation biomass using passive microwave measurements over crop fields. Remote Sens. Environ. 51, 331–341.
Wigneron, J.P., Jackson, T.J., O'Neill, P., De Lannoy, G., de Rosnay, P., Walker, J.P., Ferrazzoli, P., Mironov, V., Bircher, S., Grant, J.P., Kurum, M., Schwank, M., Munoz-Sabater, J., Das, N., Royer, A., Al-Yaari, A., Al Bitar, A., Fernandez-Moran, R., Lawrence, H., Mialon, A., Parrens, M., Richaume, P., Delwart, S., Kerr, Y., 2017. Modelling the passive microwave signature from land surfaces: a review of recent results and application to the L-band SMOS & SMAP soil moisture retrieval algorithms. Remote Sens. Environ. 192, 238–262.
Wigneron, J.P., Waldteufel, P., Chanzy, A., Calvet, J.C., Kerr, Y., 2000. Two-dimensional microwave interferometer retrieval capabilities over land surfaces (SMOS mission). Remote Sens. Environ. 73, 270–282.
Xu, L., Saatchi, S.S., Yang, Y., Yu, Y., Pongratz, J., Bloom, A.A., Bowman, K., Worden, J., Liu, J., Yin, Y., Domke, G., McRoberts, R.E., Woodall, C., Nabuurs, G.-J., Miguel, S., Keller, M., Harris, N., Maxwell, S., Schimel, D., 2021. Changes in global terrestrial live biomass over the 21st century. Sci. Adv. 7, eabe9829.
Yao, P., Lu, H., Shi, J., Zhao, T., Yang, K., Cosh, M.H., Gianotti, D.J.S., Entekhabi, D., 2021. A long term global daily soil moisture dataset derived from AMSR-E and AMSR2 (2002–2019). Sci. Data 8, 143.
Zhao, T., Hu, L., Shi, J., Lü, H., Li, S., Fan, D., Wang, P., Geng, D., Kang, C.S., Zhang, Z., 2020a. Soil moisture retrievals using L-band radiometry from variable angular ground-based and airborne observations. Remote Sens. Environ. 248, 111958.
Zhao, T., Shi, J., Entekhabi, D., Jackson, T.J., Hu, L., Peng, Z., Yao, P., Li, S., Kang, C.S., 2021. Retrievals of soil moisture and vegetation optical depth using a multi-channel collaborative algorithm. Remote Sens. Environ. 257.
Zhao, T., Shi, J., Lv, L., Xu, H., Chen, D., Cui, Q., Jackson, T.J., Yan, G., Jia, L., Chen, L., Zhao, K., Zheng, X., Zhao, L., Zheng, C., Ji, D., Xiong, C., Wang, T., Li, R., Pan, J., Wen, J., Yu, C., Zheng, Y., Jiang, L., Chai, L., Lu, H., Yao, P., Ma, J., Lv, H., Wu, J., Zhao, W., Yang, N., Guo, P., Li, Y., Hu, L., Geng, D., Zhang, Z., 2020b. Soil moisture experiment in the Luan River supporting new satellite mission opportunities. Remote Sens. Environ. 240, 111680.
Zhao, T.J., Zhang, L.X., Shi, J.C., Jiang, L.M., 2011. A physically based statistical methodology for surface soil moisture retrieval in the Tibet plateau using microwave vegetation indices. J. Geophys. Res.-Atmos. 116.
Zheng, J., Zhao, T., Lü, H., Shi, J., Cosh, M.H., Ji, D., Jiang, L., Cui, Q., Lu, H., Yang, K., Wigneron, J.-P., Li, X., Zhu, Y., Hu, L., Peng, Z., Zeng, Y., Wang, X., Kang, C.S., 2022. Assessment of 24 soil moisture datasets using a new in situ network in the Shandian River basin of China. Remote Sens. Environ. 27.